Journal of Physics and Chemistry of Solids 196 (2025) 112298

Contents lists available at ScienceDirect

Journal of Physics and Chemistry of Solids

journal homepage: www.elsevier.com/locate/jpcs

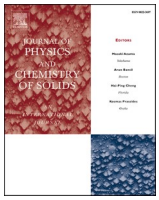

Prediction of X_2AuYZ_6 (X = Cs, Rb; Z = Cl, Br, I) double halide perovskites for photovoltaic and wasted heat management device applications

S. Mahmud [a,b,*], M.M. Hossain [a], M.M. Uddin [a], M.A. Ali [a,**]

[a] Advanced Computational Materials Research Laboratory, Department of Physics, Chittagong University of Engineering and Technology (CUET), Chattogram, 4349, Bangladesh

[b] Department of Electrical and Electronic Engineering, Jatiya Kabi Kazi Nazrul Islam University (JKKNIU), Mymensingh, 2224, Bangladesh

ARTICLE INFO

Keywords:
X_2AuYZ_6 (X = Cs, Rb; Z = Cl, Br, I)
Stability
Opto-electronic properties
Figure of merit
Thermo-dynamic properties

ABSTRACT

We used density functional theory to study the phase stability, the opto-electronic properties, and the thermo-electric behavior of X_2AuYZ_6 (where X = Cs, Rb, and Z = Cl/Br/I) double halide perovskites. The compounds belong to the cubic perovskite arrangement and are verified by the tolerance and octahedral factor. Formation enthalpy and binding energy primarily meet the requirements for structural stability. The positive frequency of phonon dispersion shows that all compounds are dynamically stable except for Rb_2AuYI_6. The negative formation energy considering the competing phase also confirmed that all compounds are thermodynamically stable. The Pugh's ratio, Poisson's ratio, and Cauchy pressure validated their ductile nature in the analysis of thermo-mechanical behavior. The electronic characteristics of Cs_2AuYZ_6 (Rb_2AuYZ_6) [Z = Cl, Br, I] double halide perovskites (DHP) have been investigated using the TB-mBJ technique, yielding band gap values of 2.85 (2.91), 2.35 (2.40), and 1.74 (1.78) eV, in that order. The optical properties are calculated, revealing the maximum absorption coefficients with respect to wavelength in the visible range of the titled compounds are 0.23 (0.35) × 10^5 cm^{-1}, 1.01 (1.06) × 10^5 cm^{-1}, and 1.42 (1.48) × 10^5 cm^{-1}, respectively, indicating their potential for photovoltaic applications. The thermo-electric transport properties were also studied. The investigated compounds [Cs (Rb)-based] exhibit ZT values of 0.51 (0.55), 0.53 (0.62), and 0.58 (0.75) at room temperature with Cl, Br, and I, respectively. As a result, the studied compounds, particularly those Rb-based with halides, have significantly greater potential than Cs in thermoelectric fields. So, among the compounds, X_2AuYI_6 (X = Cs, Rb) shows the most promise for the technological applications mentioned above due to its lower band gap, high absorption coefficient, and high ZT value.

1. Introduction

The global energy problem is getting worse due to daily consumption. The combustion of fossil fuels, such as coal, oil (petroleum), and natural gas, has contributed to environmental problems like air pollution and climate change by releasing carbon dioxide and other pollutants into the atmosphere for many years. To lessen these negative environmental effects, attempts are made to switch to greener and more sustainable energy sources. The two alternative energy sources are sunlight and waste heat, which may be used in photovoltaic and thermo-electric processes. The material selection influences the ability to execute thermal and photoelectric applications. Developing novel solar cell materials and technologies with significant efficiency, strong inherent stability, and less costly manufacturing is essential to the industry. The aforementioned procedures are of tremendous importance to perovskite halide materials. Perovskite halides, which offer a flexible platform for various applications with solar energy at the forefront, constitute a paradigm shift in materials research. The general structure of such perovskite is represented as ABX_3 or A_2BX_6, called single or double perovskite (DP), respectively, with the A cation positioned at the corner, the B cation at the center, and the X anion at the face center. A single perovskite can only tolerate the 2^+ cationic arrangement in B-sites, whereas a double perovskite can manage a wide range, from 1 to 4^+ [1]. This is why the double perovskite offers improved

* Corresponding author. Advanced Computational Materials Research Laboratory, Department of Physics, Chittagong University of Engineering and Technology (CUET), Chattogram, 4349, Bangladesh.

** Corresponding author.

E-mail addresses: shuaib.eee.iu@gmail.com (S. Mahmud), ashrafphy31@cuet.ac.bd (M.A. Ali).

https://doi.org/10.1016/j.jpcs.2024.112298
Received 11 July 2024; Received in revised form 19 August 2024; Accepted 30 August 2024
Available online 1 September 2024

functionalities, tunability properties, enhanced stability or long-term application, reduced defect density, and flexibility in band gap engineering.

The PCE (power conversion efficiency) of oxide-based perovskites has increased by about 21%, indicating their increased efficiency for solar applications [2]. The hybrid halide, or organic-inorganic lead halide, is the most studied material for advancing solar cell technology due to its high power conversion efficiency of 3–22% from 2009 to date [3–6]. However, toxicity and instability are the two fundamental problems with lead-based halide compounds. Monovalent and trivalent elements substitute the toxic element of the Pb^{2+} ion to balance the B-site and form the double perovskite structure $A_2^{+1}B^{+1}B^{+3}X_6$, thereby resolving the problems. It has been discovered that lead-free double perovskites exhibit higher solar efficiency (to 30.95%) and are safe for use while being more stable at appropriate temperatures and humidity levels than single perovskites [7].

Extensive research has been carried out on inorganic lead-free double perovskite materials having the chemical formula $Cs/Rb_2B^+B^{3+}X_6$, where B^+ represents Ag^+, Au^+, Tl^+, and B^{3+} represents Bi^{3+}, Sb^{3+}, In^{3+}, and X represents I^-, Br^-, Cl^- [8–12]. Such substances have a lot of potential to improve technological advances in many different fields and may produce environmentally friendly and productive gadgets. For example, E. T. McClure et al. [13] studied $Cs_2AgBiCl_6$ and $Cs_2AgBiBr_6$ with indirect band gaps of 2.77 eV and 1.95 eV, respectively. These band gaps surpass the Shockley-Queisser band gap limit for the optimal performance of solar cells, leading to efficiency reductions of up to 2.5%. A. J. Kale et al. [14] presented the DFT analysis of $Cs_2AuBiCl_6$ for a single junction solar cell with a band gap of 1.40 eV and a PCE of 22.18%. A. U. Haq et al. [15] examined the optoelectronic and thermal behavior of the Rb_2XGaBr_6 (X = K, Na) compound, revealing electronic band gap values of 1.90 and 2.2 eV, respectively. S.A. Aldaghfag et al. [16] determined the direct band gap values of 3.65 and 3.63 eV for $K_2ScAgCl_6$ and $Na_2ScAgCl_6$, respectively, as sunlight-absorbing materials and UV photodetectors. Recently, lead-free perovskites of Cs_2AgBiX_6 (X = Cl, Br, and I) and Cs_2AgSbX_6 (F, Cl, Br, and I) have gained appeal due to their capacity to handle some of the most significant issues, such as band gap tuning and toxicity [17–23]. Some perovskites exhibit excellent stability in the air, but their outsized band gap values (over 2.2 eV) reduce their photovoltaic capacity [24,25]. In a recent study, the authors (S. Mahmud et al. [26]) explored A_2AuScX_6 (X = Cl, Br, and I) double halide perovskites and found that they had a desirable visible band gap of 1–2 eV. These perovskites also exhibited high light absorption (10^6 orders), making them suitable for converting light into electrical power. The results on the PCE of Au-based DP with a changing B-site element, $Cs_2AuBiCl_6$ [14], influence us to search for new Au-based DPs with a band gap of around the Shockley-Queisser (S.Q.) limit [27], from which a significant PCE is expected.

Besides PV, many researchers have studied Pb-free double perovskite materials for thermo-electric applications, which convert waste heat into electricity. When a thermoelectric material achieves a ZT value of 1.0, it is considered to be operating at an exceptionally high efficiency when turning heat into electricity. Remarkably, halide DP materials have mostly been explored for photonic applications, with less experimental attention given to their thermoelectric efficiency despite their poor heat conductivity owing to their cation structure and high charge mobility. Nonetheless, research into the thermoelectric capabilities of halide perovskites is becoming increasingly popular. Several DPs, including Cs_2AgBiX_6 (X = Cl, Br) [28], Cs_2ScTlX_6 (X = Cl, Br, I) [29], and Cs_2AuScI_6 [26], exhibited figure of merit (ZT) values for thermoelectric applications at room temperature, which were approximately 0.75, 0.60, and 0.62, respectively. These prospective results encourage us to search for new potential DPs with a high ZT value.

We selected the six halide compounds. This study showed that X_2AuYZ_6 (X = Cs, Rb, Z = Cl, Br, and I) covers the UV–to-visible band gap range of 2.91 to 1.74 eV, while X_2AuYI_6 (X = Cs, Rb) has a narrow band gap value of less than 2.2 eV, potentially making them suitable for photovoltaic purposes in renewable energy devices. The cationic combination of Y and Au at the B site offers two main advantages: achieving a broad-to-narrow band gap and reducing toxicity.

Among the selected compounds, Cs_2YAuX_6 (X = Cl, Br) has been studied by Ahmad Ayyaz et al. [30]. Their study revealed a band gap of 2.2 and 2 eV, lattice thermal conductivity of 125.8 and 113.2 $Wm^{-1}K^{-1}$ (which results in negative ZT values), and ZT value of 0.76 and 0.79 at 300 K for Cs_2YAuCl_6 and Cs_2YAuBr_6, respectively. We attempted to reproduce the results by setting their input parameters (with elastic) and obtained the band values of 2.91 and 2.38 eV, lattice thermal conductivity of 0.3505 and 0.3629 $Wm^{-1}K^{-1}$, and ZT values of 0.19 and 0.14 for the same compounds. The lattice conductivity (125.8 and 113.2 $Wm^{-1}K^{-1}$) is likely unusual when we compare the results with other compounds belong to the double perovskite family. For example, the following double perovskites: Cs_2AgBiX_6 (X = Cl/Br) [31], Rb_2CuSbX_6 (X = Cl/Br/I) [32], Tl_2SeCl_6 [33], and Cs_2PtI_6 [34], have the reported lattice thermal conductivity values of 0.078/0.065 $Wm^{-1}K^{-1}$, 0.4/0.55/0.78 $Wm^{-1}K^{-1}$, 0.70 $Wm^{-1}K^{-1}$, and 0.15 $Wm^{-1}K^{-1}$ at 300 K. Therefore, the inclusion of Cs_2YAuX_6 (X = Cl, Br) perovskites is also scientific for the present study.

Hence, the objectives of this study are to comprehensively evaluate the thermodynamic phase stability, electronic, thermoelectric transport, optical, and thermo-mechanical characteristics of the aforementioned double-halide perovskites. The results of this research will provide vital knowledge on the potential of this material as an absorber for photovoltaic technology as well as thermoelectric applications. Additionally, it will open up opportunities for future investigations into its appropriateness and feasibility.

2. Computational technique

The computations were performed using the full potential linearized augmented plane wave (FP-LAPW) approach, which is based on density functional theory (DFT) and implemented in the WIEN2k code [35]. The LAPW approach separates the unit cell of materials into two regions: the interstitial area, which uses plane waves, and the atomic sphere (also known as the muffin tin), which expands wave functions. First, the structural optimization (E-V) was found using the GGA-PBE (Generalized Gradient Approximation-Perdew Burke Ernzerhof) method [36] with the 12 × 12 × 12 k point. We set the initializing parameters as follows: $RMT^*K_{max} = 8$, $G_{max} = 14$, charge convergence = 10^{-5} Ry, and energy convergence = 0.0001e. After optimization, we obtain structural entities such as the lattice parameter, bulk modulus, minimum volume, and energy by fitting the Vinet-Rose equation of state [37]. Secondly, the TB-mBJ (Trans Blaha modified-Becke-Johnson) approach was used to get a more reliable opto-electronic band gap that was close to experimental and time-efficient [38]. The spin-orbit coupling method (TB-mBJ + SOC) was used to accurately clarify band gap measurement. The thermo-electric properties were calculated using the Boltzmann transport theory and the Boltztrap2 code [39]. Thermo-elastic characteristics were studied using the IR-elast package [40]. Furthermore, we utilized the CASTEP code to verify the band gap values using the HSE-06 functional, and to calculate the phonon dispersion and associated partial DOS using the finite displacement method (FDM) [41].

3. Results and discussion

3.1. Structural properties and stability criteria

Fig. 1 illustrates the atomic 3D arrangement of the cubic crystal unit cell of Cs and Rb-based halides with Cl, Br, and I. The unit cells are face-centered, with the Fm-3m (#225) space group. The corner-sharing element of Cs/Rb and the other octahedral elements of Au and Y occupy the positions of 8c (1/4, 1/4, 1/4), 4a (1/2, 1/2, 1/2), and 4b (0, 0, 0), while halide (Z) ions are positioned at 24e (1/4, 0, 0), respectively. Firstly, we estimated the ground state structure entity using the GGA-

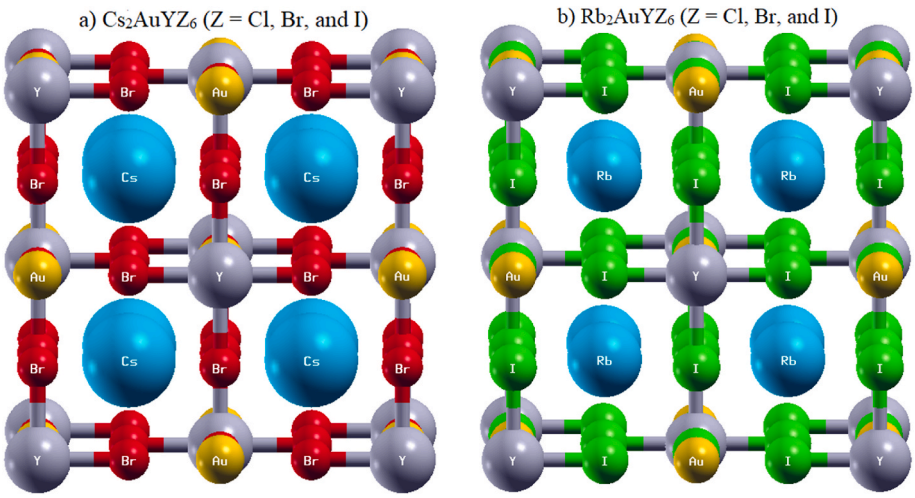

Fig. 1. Optimized unit cell of a) Cs_2AuYZ_6; and b) Rb_2AuYZ_6 [3D structure].

PBE approximation and the volume optimization method, as presented in Table 1. We employ the Vinet-Rose equation of state [37] to fit the unit cell energy vs. volume data, as shown in Fig. S1 (supplementary). The lattice parameter increases from 10.7811 (10.7261) to 11.3529 (11.2605) Å and 12.1495 (12.0988) Å for Cs_2AuYZ_6 (Rb_2AuYZ_6) as the halide (Z) ionic radius increases, leading to a decrease (less negative) in binding energy. As the lattice parameter and bulk modulus are inversely connected, the bulk modulus decreases from 32.10 (33.25) to 27.35 (27.64) GPa and 22.19 (22.75) GPa for the studied halides (Cl, Br, and I) of Cs (Rb) series materials. Furthermore, the compounds have four formula units in the ratio of 2:1:1:6.

Then, we begin by assessing the materials' structural stability using several stability index factors. Generally, double perovskites (DP) with the usual equilibrium $X_2BB'Z_6$ follow a typical cubic crystal shape. However, this perfect structure might not always be the case because of size or dimension effects, distortion of octahedral geometry, and changes in Z and J-T (Jahn-Teller) effects [42,43].

The key parameter of the cubic sign or structural stability compound is ensured by its tolerance (T_F) and octahedral factor (μ), which are calculated by the following equations of Goldsmith [44]:

$$T_F = \frac{R_X + R_Z}{\sqrt{2}\left(\frac{R_{B'}+R_{B''}}{2} + R_Z\right)}$$

$$\mu = \frac{R_{B'} + R_{B''}}{2R_Z}$$

Where R denotes the RD Shannon ionic radius of the corresponding elements, X = Cs^+/Rb^+ with coordination number 12, $R_{B'} = Au^+$, $R_{B''} = Y^{3+}$, and $R_Z = Cl^-/Br^-/I^-$ with coordination number 6 [45]. Goldsmith finds that the tolerance and octahedral factor ranges are 0.80–1.1 [46] and $0.414 < \mu < 0.89$ [47] for structural stability.

The difference between total energy and the added energy of each element per atom measures the formation energy, and the difference between total energy and the added free state energy of each element measures the binding energy. The negative values of formation and binding energies confirm the stability issues, and more negative values indicate better stability. The following equations were considered for the calculation of formation and binding energy by the element [48]:

$$\Delta H_f = \left[E_{X_2AuYZ_6} - (aE_X + bE_{Au} + cE_Y + dE_Z)\right] / N$$

$$\Delta H_b = \left[E_{X_2AuYZ_6} - (a\mu_X + b\mu_{Au} + c\mu_Y + d\mu_Z)\right] / N$$

Where the compound's total energy with Z = Cl, Br or I atoms is represented by $E_{X_2AuYZ_6}$. The amount of energy of each atom is shown by the symbols E_X, E_{Au}, E_Y and E_Z while a, b, c, and d refer to the number of atoms of Cs/Rb, Au, Y, and Cl/Br/I in the unit cell or compositions, respectively. The formation energy goes up from −2.45 (−2.41) eV to −2.07 (−2.02) eV and −1.62 (−1.57) eV for Cs (Rb) with Cl, Br, and I atoms, which shows that the stability is going down. Also, the binding energy increases with decreasing stability from −4.18 (4.16) to −3.81 (3.78) eV and −3.41 (3.37) eV due to the increasing halide ion substitution for the same atom, respectively.

Fig. 2(a–f) shows the well-calibrated phonon band structures and corresponding total density of states (TDOS) along with partial density of states (PDOS) for six different materials: Cs_2AuYCl_6, Cs_2AuYBr_6, Cs_2AuYI_6, Rb_2AuYCl_6, Rb_2AuYBr_6, and Rb_2AuYI_6 were used to check the dynamic stability. The horizontal axis in each plot represents the high-symmetry points in the Brillouin zone, and the vertical axis represents the phonon frequency in THz. On the right side of each plot, the total density of states (TDOS) and partial density of states (PDOS) for each atom type are shown. These describe how phonons in a crystalline

Table 1
Structural parameters of Cs_2AuYCl_6, Cs_2AuYBr_6, Cs_2AuYI_6, Rb_2AuYCl_6, Rb_2AuYBr_6, and Rb_2AuYI_6 compounds.

Parameter	Cs_2AuYCl_6	Cs_2AuYBr_6	Cs_2AuYI_6	Rb_2AuYCl_6	Rb_2AuYBr_6	Rb_2AuYI_6
Lattice constant, $a = b = c$ (Å)	10.7811	11.3529	12.1495	10.7261	11.2605	12.0988
	10.76 [30]	11.31 [30]	–	–	–	–
Final volume, V (Bohr^3)	2114.09	2468.63	3025.59	2081.89	2408.88	2987.88
Tolerance factor, T_F	0.88	0.87	0.86	0.85	0.84	0.83
Octahedral factor, μ	0.62	0.57	0.51	0.62	0.57	0.51
Formation energy, ΔH_f (eV/atom)	−2.45	−2.07	−1.62	−2.41	−2.02	−1.57
Binding energy, ΔH_b (eV/atom)	−4.18	−3.81	−3.41	−4.16	−3.78	−3.37
Minimum energy, E_o (Ry)	−81567.68	−107309.20	−161457.95	−62332.44	−88073.96	−142222.70
Bulk modulus, B_0	32.10	27.35	22.19	33.25	27.64	22.75
B_0'	5.14	4.60	3.12	5.49	4.36	3.17

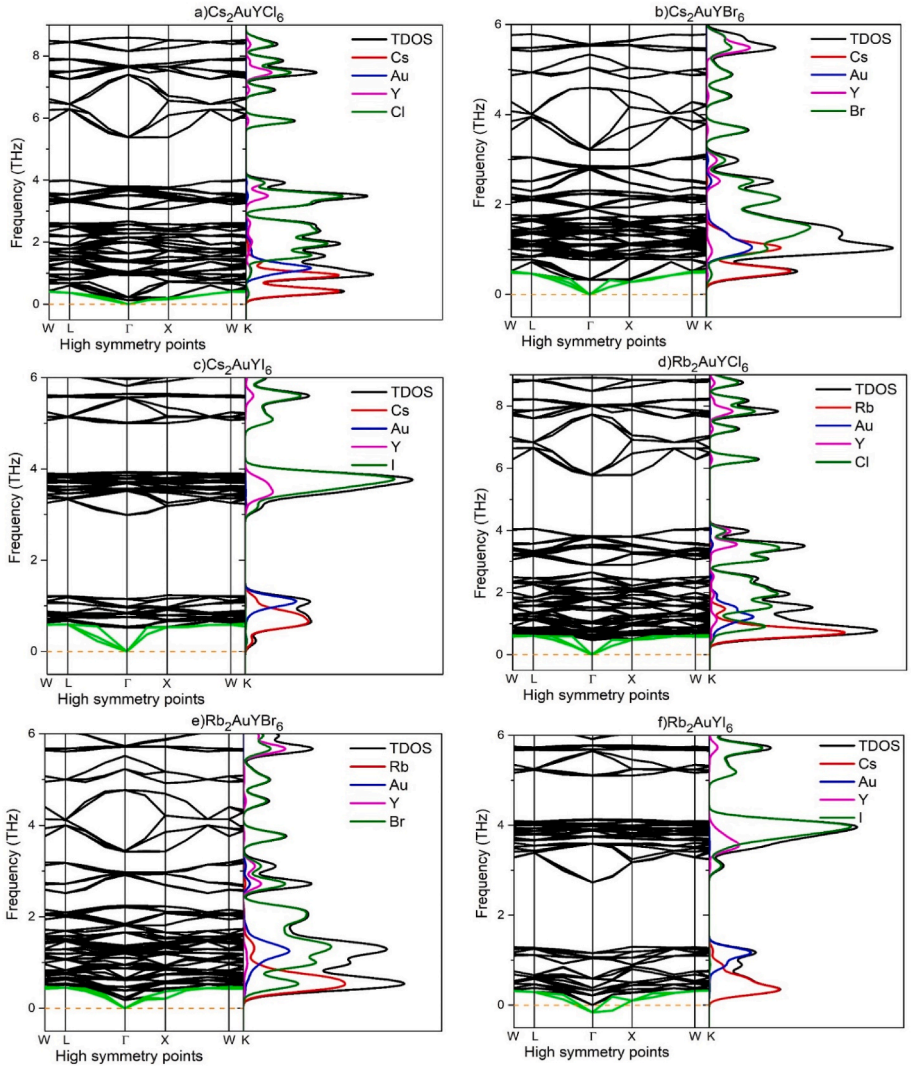

Fig. 2. Phonon band dispersion (left side) with TDOS and PDOS (right side) of a) Cs_2AuYCl_6, b) Cs_2AuYBr_6, c) Cs_2AuYI_6, d) Rb_2AuYCl_6, e) Rb_2AuYBr_6, and f) Rb_2AuYI_6.

material relate to one another in terms of frequency (energy) and wave vector (momentum) in the first Brillion zone. In a crystal lattice, collective atomic vibrations are represented by quanta of vibrational energy called phonons. Some important physical processes that phonons affect are heat transmission, electrical conductivity, and the thermal growth of objects. The dispersion showed a positive frequency except for Rb_2AuYI_6 with a 3 N (3 × 40) vibrational mode by conventional unit cell. Three of these modes, identified as the acoustic mode (green color), function solely in the low-frequency region to converge gamma points. In contrast, the remaining modes, known as the optic mode, operate in the higher-frequency region (black color).

In **Fig. 2(a)**, the lowest phonon modes are relatively flat and lie close to 0 to 1 THz, indicating low-frequency vibrations primarily associated with the heavier Cs and Au atoms. The modes are split into several optical branches, with the highest reaching up to approximately 9 THz. From the partial DOS of the phonon, the Cl element, in conjunction with a slightly Y atom, dominates the band structure of the phonon in the higher part of the frequency range with a phononic gap between 4 and 5.5 THz. In Fig. 2(b), the lowest acoustic part (close to zero) and optic part (≈1 THz) are flat for heavy atoms (Cs, Au, and Br). The upper part of the optic mode (above 1 THz) is dominated by the Br atom in the dispersion curve, which is reflected in the PDOS of Cs_2AuYBr_6. In **Fig. 2 (c)**, the lowest modes remain near 0 THz, but the overall phonon frequencies are reduced, with the highest modes reaching about 6 THz. The bands are more closely spaced compared to the Cl and Br analogues, indicating a more condensed phonon spectrum due to the heavier I atoms. There is a clear phononic gap between 1 to 3 THz and 4 to 5 THz, which is clear evidence in the PDOS of Cs_2AuYI_6. In **Fig 2(d-e-f)**, the dispersion curves show maximum similarities to Cs_2AuYCl_6, Cs_2AuYBr_6, and Cs_2AuYI_6, respectively, but with a slightly broader or flat peak with a low frequency range (less than 1 THz), likely due to the replacement of Cs with the slightly lighter Rb, which indicates higher scattering than Cs-based compounds.

There is a larger phononic gap or phase space in both I-based compounds than in the others, which might result from phonon heat being restricted due to high phonon scattering. Impurities, phonons, surfaces, or electrons cause the scattering of phonons. The interaction of electrons and phonons in semiconductors is negligible. The high phonon scattering indicates lower phonon group velocity and reduced thermal conductivity [31,34], which is shown in the thermoelectric section of Fig. 5(d).

Although the band dispersion curve of the Rb_2AuYI_6 compound has a small negative value for acoustic mode (which also seems to be in the DOS curve), the mechanical criteria (supplementary section) and the formation energy by element and competing phase strongly suggest the mechanical and thermo-dynamic stability of that compound. So, the

studied compounds are considered synthesizable as they meet the following criteria: tolerance and octahedral factor of a certain range, the negative value of formation and binding energy, and the negativity of competing phases.

The chemical or thermo-dynamic stability may be calculated by its phase stability. Understanding phase stability is crucial in materials science, chemistry, and engineering because it helps in predicting material behavior and designing materials for specific applications. The possible identified competing phases are shown on the right side of the equation of Cs and Rb-based halides with the help of the open quantum materials database (OQMD) [49].

For Cs based halides, $Cs_2AuYZ_6 \rightarrow \frac{1}{4}\ CsAuZ_3 + \frac{7}{10}Cs_3Y_2Z_9 + \frac{1}{20}Au$

For Rb based halides, $Rb_2AuYZ_6 \rightarrow \frac{1}{4}\ RbAuZ_3 + \frac{1}{2}Rb_3YZ_6 + \frac{1}{5}YZ_3 + \frac{1}{20}Au$

The possible phases of $CsAuCl_3$, $CsAuBr_3$, and $CsAuI_3$, as well as the prototype of $Cs_3Cr_2Cl_9$, are used for Cs-based halides (Cl, Br, and I), while the phases of $RbAuCl_3$, $RbAuBr_3$, $RbAuI_3$, Rb_3YCl_6, Rb_3YBr_6, Rb_3YCl_6, YCl_3, YBr_3, YI_3, and Au are used for Rb-based halides (Cl, Br, and I) to determine the stability of each of the studied compounds. These compounds structure are taken from the materials project [50] for the calculation of each formation enthalpy. If any path of formation enthalpy is positive, no stable region is possible in the phase diagram. So, the formation enthalpy of each identified phase must be negative. All compounds and phases show a negative value, indicating the chemical stability of the studied compound (see Table 2).

3.2. Electronic properties, effective mass of charge carrier, and density of states

DFT calculations can provide insights into these materials' band structure, mobility, density of states, and other electronic properties. Whether a material is an insulator, conductor, or semiconductor depends on how its electrons are distributed throughout their energy levels, as described by its band structure [51]. The basic need for realizing optical and thermoelectric characterization is also to understand the electronic band structure. Determining the band gap, or the energy difference between the highest and lowest unoccupied states, is essential to comprehending the electrical characteristics of the material. The composition of the band profile is displayed in Fig. 3. The band structure was calculated by four processes: The first is the GGA-PBE SCF calculation, and the second is the TB-mBJ SCF calculation. The band gap values of the GGA-PBE approach are 2.05 (2.07), 1.56 (1.60), and 1.05 (1.07) eV, and those of the TB-mBJ approach are 2.85 (2.91), 2.35 (2.40), and 1.74 (1.78) eV for Cs (Rb) based on halides of Cl, Br, and I, respectively. The GGA-PBE functional always shows an underestimated value with correctly constructed structural features, and the TB-mBJ functional is widely recognized and close to the experimental value. The reported band gap values of Cs_2AuYCl_6 and Cs_2AuYBr_6 are 2.2 eV and 2 eV, respectively, exhibiting a difference of 0.65 eV and 0.35 eV

Table 2
Formation enthalpy for chemical stability.

Compound	Phases	Formation enthalpy by competing phase (meV/atom)	Formation enthalpy of each phase (eV/atom)
Cs_2AuYCl_6	$CsAuCl_3$, $Cs_3Y_2Cl_9$	−25	−1.67, −2.90
Cs_2AuYBr_6	$CsAuBr_3$, $Cs_3Y_2Br_9$	−18	−1.43, −2.45
Cs_2AuYI_6	$CsAuI_3$, $Cs_3Y_2I_9$	−12	−1.16, −1.90
Rb_2AuYCl_6	$RbAuCl_3$, Rb_3YCl_6, YCl_3	−17	−1.52, −2.77, −3.20
Rb_2AuYBr_6	$RbAuBr_3$, Rb_3YBr_6, YBr_3	−10	−0.86, −2.38, −2.70
Rb_2AuYI_6	$RbAuI_3$, Rb_3YI_6, YI_3, Au	−05	−1.03, −1.80, −2.00, 0

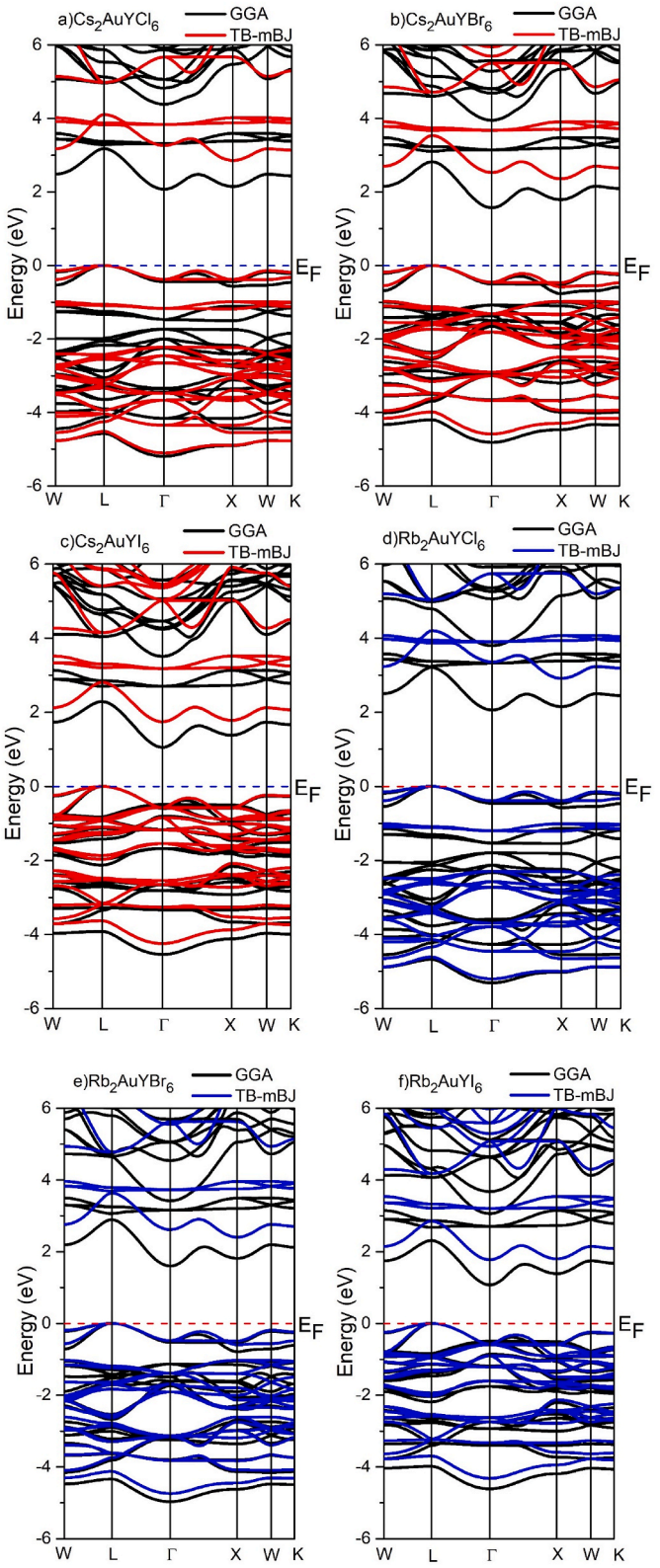

Fig. 3. Electronic band structure of a) Cs_2AuYCl_6, b) Cs_2AuYBr_6, c) Cs_2AuYI_6, d) Rb_2AuYCl_6, e) Rb_2AuYBr_6 and, f) Rb_2AuYI_6; computed by GGA-PBE (Black color) and TB-mBJ (Red and blue) approach.

compared to our findings [30]. In order to verify the accuracy of our results, we reproduced the results for many compounds, including $Cs_2ScInBr_6$, Rb_2AgBiI_6, and $Cs_2CuBiCl_6$, using the TB-mBJ approach, which showed a precise match of 0.805, 1.219, and 1.20 eV with reported data of 0.81 [52], 1.22 [53], and 1.19 eV [54], respectively, as shown in Table 3. Thirdly, the band structures computed using TB-mBJ + SOC exhibit slightly increased or decreased values (insignificant variation) for the sake of clarification and for convenience. These results show a reasonable degree of agreement with similar studies [26,55]. Lastly, we also accomplished the band gap values by using HSE-06 functional, and the band gap values obtained were 3.03 (3.09), 2.48 (2.52), and 1.88 (1.92) eV, which are more consistent with the TB-mBJ approach (see Fig. S2 in supplementary information). So, to determine the exact band gap in the present findings, the TB-mBJ potential (commonly mBJ potential) is used, which is more time-efficient than the hybrid function HSE-06. The outcomes of the HSE-06 potentials exhibit slightly increased band gap values due to the use of different potentials, although the studied compounds are mostly comparable in line with other findings such as $Ag_2BaGeSe_4$ (mBJ- 0.909 eV, HSE06–0.85 eV), $Ag_2BaSnSe_4$ (mBJ- 0.832 eV, HSE06–0.77 eV), $Ag_2SrGeSe_4$ (mBJ- 0.708 eV, HSE06–0.68 eV), and $Ag_2SrSnSe_4$ (mBJ- 0.729 eV, HSE06–0.66 eV) [56].

Compared to the GGA-PBE strategy, the TB-mBJ and HSE-06 approaches for each compound eliminate the degeneracy of certain states, increasing the band gap values. The band gap value from Cl to I decreases due to the overlapping states caused by the increasing size of halogens. This may happen due to the decreasing contribution of Au-*d* and Z-*p* in the valence band, and consequently, the gap decreased by Y-*d* and Au-*s* in the conduction band. Notably, I-based compounds have band gaps within a narrow range (1–2 eV), making them useful semiconductors for turning solar energy into electrical power. Additionally, the reported band gap value of $Cs_2TlBiBr_6$ (2.32 eV) is lower than that of $Cs_2TlBiCl_6$ (2.89 eV), confirming the correctness of our computation [57]. The all-compound exhibits an indirect band gap due to different symmetry points (L-X) when considering the lowest state in CB and the highest state in VB for the TB-mBJ, TB-mBJ + SOC, and HSE-06 approaches. As a result, the electronic transition from VB to CB occurs, possibly with the assistance of phonons (lattice vibration), leading to lower recombination rates [58]. This may lead to longer carrier lifetimes, making them suitable for certain applications where non-radiative recombination must be kept to a minimum. However, the presence of phonons is unfavorable as it increases heat loss during device operation [59].

The electronic band gap threshold energy, which is smaller than the optical absorption energy, demonstrates the indirect band gap. Reference [60] reported similar observations. Besides, the indirect band gap materials may be easier to integrate into current semiconductor devices and circuits since they are more compatible with silicon technology. Additionally, materials with an indirect band gap might have improved thermal stability, making them appropriate for high-temperature or harsh environmental uses.

The effective mass of charge carriers, like electrons or holes, describes their behavior as mass-specific free particles. The crystal lattice impacts charge carriers in crystalline solids, leading to complicated behaviors. The effective mass helps to simplify this difficult situation by treating charge carriers as if they were flowing in a gas of free electrons or holes with a fixed effective mass. First, analyze the band structure to determine the curvature near the band edges to achieve this. The second derivative of the energy (E) with respect to momentum (K), i.e., d^2E/dK^2, must represent the curvature, and the inverse of this curvature then yields the effective mass [61]:

$$m^* = \frac{\hbar^2}{\left(d^2E/dK^2\right)}$$

Where, $\hbar = 1.05 \times 10^{-34}$ J/s. The estimated values of effective mass and holes are also presented in Table 3. The fact that the effective mass of holes is higher than that of electrons indicates p-type materials due to planar states in VB and high curvature in CB, which is advantageous for making green energy and optoelectronic devices [62,63]. Furthermore, CB exhibits a greater dispersion pattern than VB, which improves the thermoelectric effectiveness of the materials under study. It is observed that the effective mass values show a significant degree of consistency with other similar findings [26], and the values are low compared with other reported values of Cs_2AgSbX_6 (X = Cl, Br, and I) [21]. The reduced effective mass confers an advantage in better carrier mobility, which is an exceptionally sought-after characteristic in advancing highly effective electrical and optoelectronic systems.

Furthermore, using the subsequent charge carrier, we may determine the effective state densities of the VB and CB, designated as N_v and N_c individually [64].

$$N_v = 2\frac{\left(2\pi m_h^* k_B T\right)^{3/2}}{h^3} \approx 2.5409 \times 10^{19}\left(\frac{m_h^*}{m_0}\right)^{3/2}$$

$$N_c = 2\frac{\left(2\pi m_e^* k_B T\right)^{3/2}}{h^3} \approx 2.5409 \times 10^{19}\left(\frac{m_e^*}{m_0}\right)^{3/2}$$

Where T is the temperature in Kelvin, k_B is the Boltzmann value, and h represents the Planck constant. The values of N_v and N_c are shown in Table 3, and the computed values are very low compared to other similar types of DP materials of Cs_2TlBiX_6 (X = Cl, Br, and I) [57]. Overall, the perovskite solar-powered devices benefit from low operative state densities in both the conduction and valence bands (N_v and N_c) so as to optimize their efficacy.

Fig. S3 (supplementary part) shows total and partial DOS for forming

Table 3
Computed band gaps by different approaches, the effective masses of holes (m_h*) and electrons (m_e*), and the effective density of states for studied compounds.

Compound	Band gap (eV)				Effective masses by TB-mBJ		Effective density of states ($\times 10^{18}$ states/cm^3)		References
	GGA-PBE	TB-mBJ	TB-mBJ + SOC	HSE-06	m_h^*/m_0	m_e^*/m_0	N_V	N_c	
Cs_2AuYCl_6	2.05	2.85	2.89	3.03	0.41	0.14	6.67	1.33	This work
	1.4	2.2	–	–	0.58	0.25	–	–	[30]
Cs_2AuYBr_6	1.56	2.35	2.30	2.48	0.32	0.12	4.59	1.05	This work
	1.2	2.0	–	–	0.31	0.15	–	–	[30]
Cs_2AuYI_6	1.05	1.74	1.79	1.88	0.26	0.08	3.36	0.57	This work
Rb_2AuYCl_6	2.07	2.91	2.95	3.09	0.39	0.13	6.18	1.19	This work
Rb_2AuYBr_6	1.60	2.40	2.33	2.52	0.30	0.12	4.17	1.05	This work
Rb_2AuYI_6	1.07	1.78	1.81	1.92	0.25	0.07	3.18	0.47	This work
$Cs_2ScInBr_6$	0.712	0.805	–	–	–	–	–	–	This work
	0.73	0.81							[52]
Rb_2AgBiI_6	0.723	1.219	–	–	–	–	–	–	This work
	–	1.22							[53]
$Cs_2CuBiCl_6$	0.85	1.20	–	–	–	–	–	–	This work
	0.83	1.19							[54]

band structures from −6 eV to +6 eV. Plotting the total DOS against energy allows one to identify characteristics like the band gap and the density of states at the Fermi level. The partial DOS describes the contribution of individual atomic orbitals or elements to the total DOS, and it aids in a more thorough analysis of the bonding and electronic structure. The atomic states were similar for all of the studied atoms. At the top of the VB, the elemental participation consists of Au-*d* and Z-*p* orbitals, whereas the bottom of the CB consists of Au-*s*, Y-*d*, and Z-*p* orbitals. The Cs^{+}/Rb^{+} ions only maintain the structural stability, not the band structure of the studied compound. So, electronic insights can guide experimental efforts to tailor these materials for specific applications.

3.3. Nature of bonding

The compound X_2AuYZ_6 (Z = Cl, Br, and I) is a member of the double perovskites family. Its bonding nature may be comprehended by analyzing the properties of its component elements and their interrelationships. The relationship depends on their electronegativity and chemical bonds.

In compounds of Fig. 4, the halide ions (Z = Cl, Br, and I) have comparatively high electro-negativities, whereas Cs/Rb has a low electronegativity. Usually, an ionic connection occurs between Cs/Rb and Z when Cs/Rb gives electrons to Z, producing Z-anions and Cs^{+}/Rb^{+} cations. The high electronegativity difference between caesium and halogens predicts the X-Z bond to be predominantly ionic. Various oxidation states are possible for both yttrium and gold, and they may share electrons to create covalent connections within the structure.

The two interpenetrating networks of octahedra bonding between B-Z (Au-Z) and B′-Z (Y-Z) are likely covalent. These elements' octahedral configuration in the perovskite structure makes electron sharing easier. Specifically, the Au–Cl demonstrates a strong covalent bond, while the Au–Br and Au–I also demonstrate a less covalent bond. Meanwhile, the Y-Z exhibits a covalent bond with a weak ionic bond. A Similar result has been reported in the literature [65].

In summary, X_2AuYZ_6 exhibits a combination of ionic and covalent bonding. The bonds between the caesium, gold, yttrium, and halogen (Z) atoms give this double perovskite structure its unique properties and stability. The bonding characteristics may vary slightly depending on the specific halogen present (Cl, Br, and I), but the general trends mentioned above remain applicable.

3.4. Thermoelectric transport properties

The ability to efficiently convert waste heat into useable electrical power and vice versa is a crucial feature of the transport or thermoelectric property, which has many real-world applications in a variety of industries, promotes energy sustainability, and helps to solve energy-related problems. Band structure in semiconductors determines the different transport parameters, with the band gap from Fermi-level, type of carrier concentration, and carrier effective mass values making the most significant contributions [66].

To investigate the suitability of compounds for device applications, it is essential to examine their transport properties by considering TB-mBJ Fermi energy. The BoltzTraP2 code incorporates a fixed relaxation time (τ) set at 10^{-14} s for all thermoelectric applications [39]. In the temperature range of 100–1000K, the temperature-dependent variables of electrical conductivity (σ/τ), carrier concentration (N), and electronic conductivity (k_e/τ) are calculated and presented in Fig. 5(a–c).

Electrical conductivity characterizes the ability of the material to conduct electricity. A rise in carrier concentration (N) causes an upward trend in electrical conductivity as a function of temperature. It may be

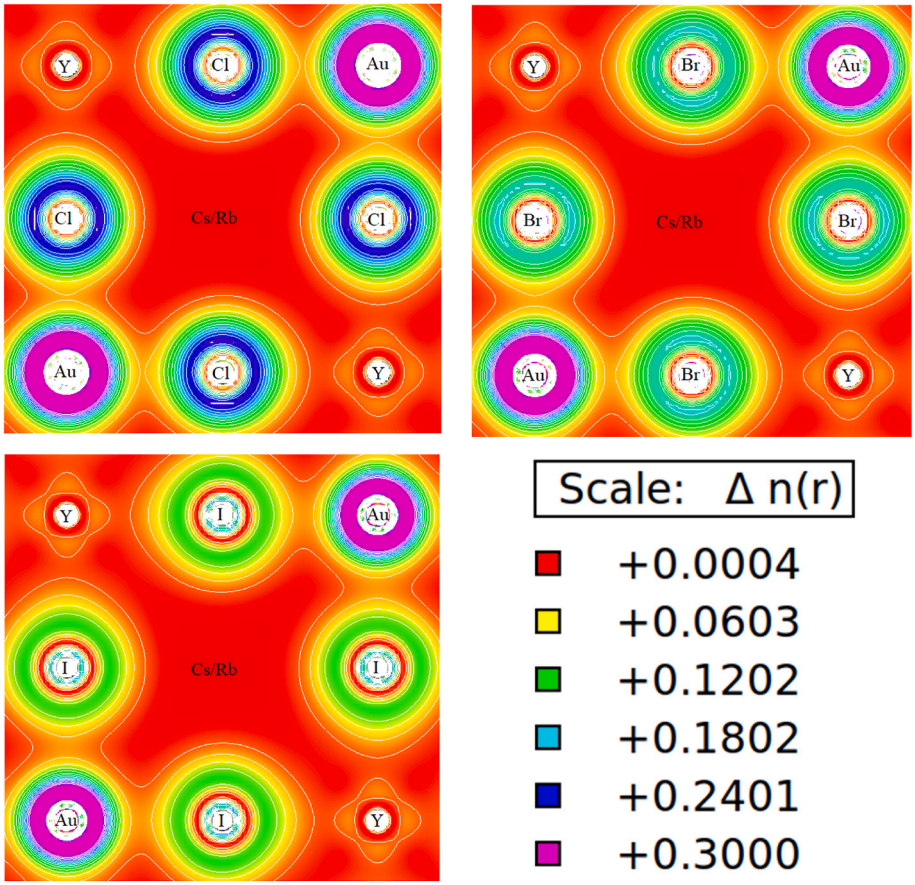

Fig. 4. Charge density mapping of Cs/Rb_2AuYCl_6, Cs/Rb_2AuYBr_6, and Cs/Rb_2AuYI_6.

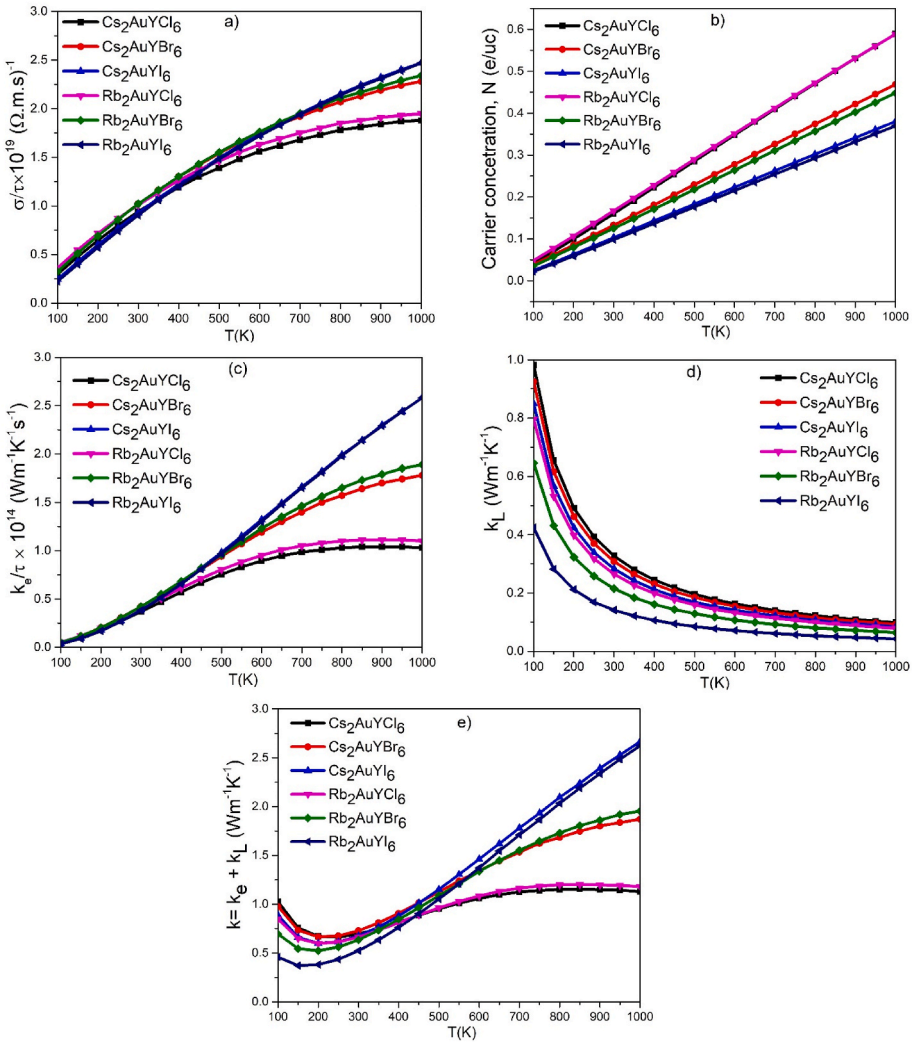

Fig. 5. The computed a) σ/τ: Electrical conductivity, b) N: Carrier concentration, c) k_e/τ: electronic thermal conductivity, d) k_L: Lattice thermal conductivity, and e) k: Total thermal conductivity, of Cs_2AuYCl_6, Cs_2AuYBr_6, Cs_2AuYI_6, Rb_2AuYCl_6, Rb_2AuYBr_6, and Rb_2AuYI_6.

expressed as $\sigma = Ne\mu$, characteristic of semiconducting material. Furthermore, when the carrier concentration is positive, it implies that holes are contributing, and when it is negative, it shows that electrons are the main carriers [67]. As the temperature rises, the electrons acquire energy, resulting in a strong positive variation in carrier concentration. The reported σ/τ values at 300K are 0.94 (1.01) × 10^{19}, 1.02 (1.02) × 10^{19}, and 0.92 (0.90) × 10^{19} $(\Omega.m.s)^{-1}$ for Cs and Rb based on halides (Cl, Br, and I). The study has shown that, when Cl is replaced with Br and I, the value of σ increases with temperature. But in the case of I for both compounds, the value of σ crosses a certain level (350 K for Cl and 450 K for Br) and shows a higher value at high temperatures. The aforementioned compounds exhibit comparatively high electrical conductivity due to their incredibly low resistances; this suggests that they may find application in the fabrication of thermoelectric systems.

The Boltztrap2 code solely focusses on the electronic part of thermal conductivity (k_e/τ), as phonon calculations go beyond the scope. The calculated values of k_e/τ at 300K for Cs_2AuYCl_6 (Rb_2AuYCl_6), Cs_2AuYBr_6 (Rb_2AuYBr_6), and Cs_2AuYI_6 (Rb_2AuYI_6) are 0.36 (0.40) × 10^{14}, 0.42 (0.42) × 10^{14}, and 0.39 (0.38) × 10^{14} ($Wm^{-1}K^{-1}s^{-1}$), respectively. As the temperature of a material rises, the lattice vibrates progressively more, increasing the electronic component of thermal conductivity. It should be noted that a factor of 10^5 (the ratio of σ and k_e) indicates that the materials can produce thermoelectric power. The σ and k_e follow an identical pattern, relying on carrier concentration (N).

The total thermal conductivity (k) of a material may be calculated by considering the lattice thermal conductivity (k_L) and electronic thermal conductivity (k_e), where $k = k_e + k_L$. Slack's model is very popular and widely used to evaluate the k_L independently, and it can be estimated using the following formula [68]:

$$k_L = \frac{A(\gamma)\delta M_{av}\theta_D^3}{\gamma^2 n^{2/3} T}$$

A is a constant dependent on γ, δ is the mean atomic volume of the cubic root, M_{av} is the mean atomic mass, θ_D is the Debye hardness, γ corresponds to the Gruneisen parameter, n stands for the unit cell atom, and T represents the absolute temperature in kelvin. Fig. 5 (d) plots the computed value of k_L versus T and demonstrates how it decreases throughout the temperature range. Increasing temperature weakens interatomic lattice links, leading to a decrease in k_L and phonon group velocity. Besides, there is an inverse relationship between temperature and lattice thermal conductivity (k_L α $1/T$) [69,70]. The corresponding values of k_L at room temperature for Cs (Rb)-based halides are 0.32 (0.26), 0.30 (0.21), and 0.28 (0.14) $Wm^{-1}K^{-1}$, respectively, as shown in Table 4.

The overall thermal conductivity of the material under investigation is illustrated in Fig. 5(e). It first declines at low temperatures before significantly increasing between 200 and 1000 K in relation to electrical conductivity. Because of this, the Wide-man Franz law supports these

Table 4
The electrical conductivity (σ), electronic thermal conductivity (k_e), lattice thermal conductivity (k_L), power factor (S), and figure of merit (*ZT*) obtained by the TB-mBJ approach at 300 K for the studied compounds.

Compound	$\sigma \times 10^5$ (1/Ω.m)	k_e ($Wm^{-1}K^{-1}$)	k_L ($Wm^{-1}K^{-1}$)	S (μV/K)	PF $\times 10^{-3}$ ($Wm^{-1}K^{-2}$)	ZT	References
Cs_2AuYCl_6	0.942	0.368	0.327	195	3.57	0.51	This work
	–	–	125.8	–	–	0.76	[30]
Cs_2AuYBr_6	1.02	0.421	0.308	195	3.88	0.53	This work
	–	–	113.2	–	–	0.79	[30]
Cs_2AuYI_6	0.927	0.392	0.283	206	3.94	0.58	This work
Rb_2AuYCl_6	1.01	0.399	0.265	189	3.62	0.55	This work
Rb_2AuYBr_6	1.02	0.421	0.215	197	3.94	0.62	This work
Rb_2AuYI_6	0.903	0.383	0.141	206	3.95	0.75	This work

conclusions about the charge carrier or electronic conductivity and expresses their proportionate relationship as follows: $k_e = LT\sigma$ [71], where *L* is the Lorentz constant (2.44×10^{-8} W/S–K^2). However, the Rb-based compound exhibits lower thermal conductivity than Cs-based halides at ambient temperature (300K), which might have an impact on the material's efficiency.

The following equation, which considers the combined effects of carrier concentration (*N*) and effective mass (m^*), measures the see-beck coefficient (*S*) of degenerative semiconducting material [72]:

$$S = \left(\frac{8\pi^2 k_B^2}{3h^2 e}\right)\left(\frac{3N}{\pi}\right)^{-2/3} m^* T$$

Materials with a smaller band gap generally show greater S values, whereas those with a more significant band gap show lower *S* values [73,74]. Fig. 6(a) clearly illustrates the inverse connection between *S* and *N*, leading to a decrease in the S value. The values of S at room temperature for Cs_2AuYCl_6 (Rb_2AuYCl_6), Cs_2AuYBr_6 (Rb_2AuYBr_6), and Cs_2AuYI_6 (Rb_2AuYI_6) are 195 (189), 195 (197), and 206 (209) μV/K, respectively. Based on their positive *S* values, these substances are *p*-type semiconductors suitable for power generation applications.

For TE compounds and systems, the power factor is a significant factor. The symbol "PF" commonly represents the calculation, which goes like this: power factor (PF)=($S^2\sigma$). An excellent power factor indicates an efficient thermoelectric material for power-generating applications. High electrical conductivity and a high See-beck coefficient are desirable for thermoelectric materials to maximize the power factor. However, it may be difficult to optimize both features since their relationships are often inverse. The values of PF recorded at 300K are 3.57 (3.62) $\times 10^{-3}$, 3.88 (3.94) $\times 10^{-3}$, and 3.94 (3.95) $\times 10^{-3}$ ($Wm^{-1}K^{-2}$), respectively, as presented in Fig. 6(b).

The figure of merit (*ZT*) is a critical indicator for assessing how well a thermoelectric material converts heat into electricity or efficiency. The formula for the figure of merit is $ZT = S^2\sigma T/(k_e + k_L)$ [75]. This dimensionless value considers the See-beck coefficient (*S*), thermal conductivity (*k*), and electrical conductivity (σ), all of which are essential properties of a thermoelectric material. Scientists and engineers strive to find a balance that maximizes the *ZT* value; however, optimizing these features may be difficult since they often have contradictory correlations. A thermoelectric material with a higher *ZT* value (~1) is more efficient for thermoelectric applications, including waste heat generators or thermoelectric cooling systems for refrigeration.

We have calculated the *ZT* value by utilizing the electronic and lattice contributions. As a result, the dimensionless *ZT* value falls due to increased total thermal conductivity, *k*. As shown in Fig. 6(c), the highest *ZT* values were 0.51, 0.53, and 0.58 for Cs-based halides (Cl, Br, and I) and 0.55, 0.62, and 0.75 for Rb-based halides (Cl, Br, and I) at

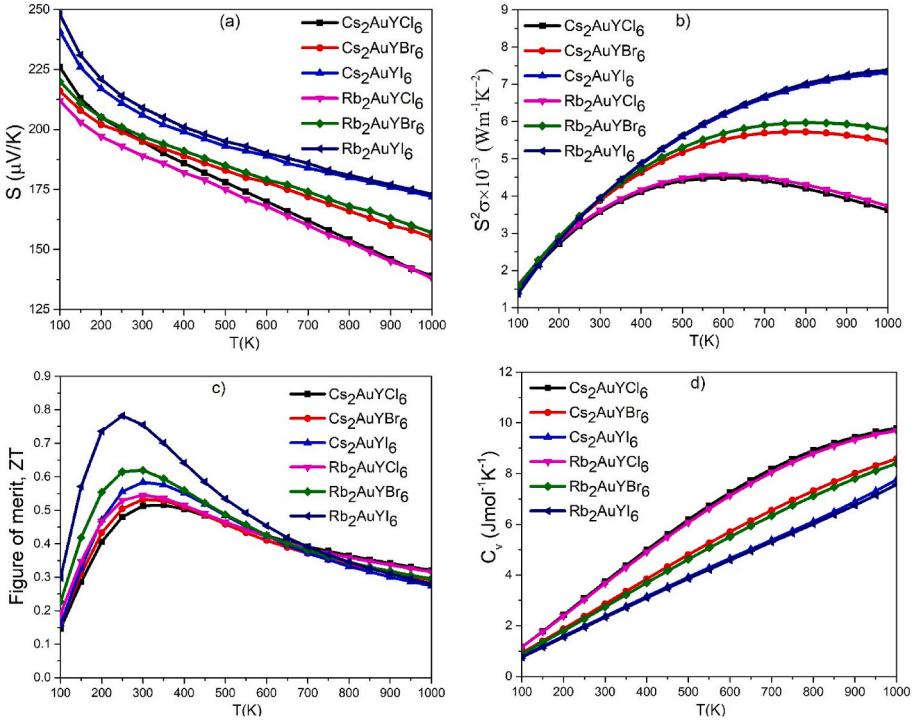

Fig. 6. a) ***S***: See-beck coefficient, b) $S^2\sigma$: Power factor, c) ***ZT***: Figure of merit, d) ***Cv***: Constant-volume specific heat of Cs_2AuYCl_6, Cs_2AuYBr_6, Cs_2AuYI_6, Rb_2AuYCl_6, Rb_2AuYBr_6, and Rb_2AuYI_6.

300K. These values are higher than those of the metal halide perovskite materials $CsSnI_3$ (ZT = 0.14) [76], $FASnI_3$ (ZT = 0.19) [77], and $CsSn_{0.8}Ge_{0.2}I_3$ (ZT = 0.12) [78]. Additionally, these outcomes are in line with comparable categories of published resources such as Cs_2AuScX_6 (X = Cl, Br, I; ZT = 0.44, 0.47, 0.62) [26], Rb_2AuScX_6 (X = Cl, Br, I; ZT = 0.47, 0.53, 0.54) [26], and Rb_2LiTlX_6 (X = Cl. Br; ZT = 0.43/0.51) [79] at room temperature, and also carry more significant value than other DPs halide materials such as Rb_2AuBiX_6 [80], Li_2CuBiZ_6 [81], Cs/Rb_2KScI_6 [82], Rb_2ScTlX_6 [24], and Cs_2InAsX_6 [83]. The reported ZT values for Cs_2AuYCl_6 and Cs_2AuYBr_6 at 500K are 0.78 and 0.82 [30], respectively, but these values are not appropriate considering their high lattice thermal conductivity, which ranges from 125.8 to 105 $Wm^{-1}K^{-1}$ and 113.2–95 $Wm^{-1}K^{-1}$ throughout the temperature range of 300–800 K. Their findings lack consistency due to the fact that similar kinds of materials exhibited very low k_L values, for example, k_L of 0.05/1.86/0.35 $Wm^{-1}K^{-1}$ for Rb_2AuBiX_6 (X = F/Cl/Br) [80] and 1.79/1.40/0.28 $Wm^{-1}K^{-1}$ for Rb_2NaTlZ_6 (Z = Cl/Br/I) [84]. We have also published our previous article on A_2AuScX_6 (A = Cs, Rb; X = Cl, Br, and I) [26], wherein the k_L values are in the range of 0.48 to 0.28 $Wm^{-1}K^{-1}$.

It should be noted that the theoretical calculation of k_L using the Slacks equation overestimates the actual value broadly [56], but in most cases, such as SnSe [85] and Ag_2XYSe_4 [56], the BTE code and experimental works have negligible differences for the calculation of lattice thermal conductivity. Therefore, we expect the experimental ZT values to exceed the values we computed. When a thermoelectric material is subjected to temperature variations, its specific heat affects its capacity to absorb or release heat. The specific heat of an ideal thermoelectric material should be as low as possible. This is because a material with a reduced specific heat becomes more responsive to changes in temperature as it requires less thermal energy to increase its temperature. The maximum value of C_v is shown for I-based composition, which rises steadily as T increases. Most solids attain their saturation value as the temperature rises above the Debye temperature; however, the highest saturation was seen for I-based compounds than for Br and Cl-based compounds in this range of temperatures, as shown in Fig. 6(d).

3.5. Optical properties

The optical properties of a material describe its response to light, directly influencing the device's performance. The optimized optical nature may be identified by the complex quantity of dielectric tensor, which is given by Ehrenreich and Cohen's equation [86]: $\epsilon(\omega) = \varepsilon_1(\omega) + i\varepsilon_2(\omega)$, where ω represents the angular frequency, $\varepsilon_1(\omega)$ and $\varepsilon_2(\omega)$ represents the real and imaginary component of dielectric tensor, calculated by the Kramers-Kronig [87] and Kohn-Shams equations [88], which are responsible for the polarization and light absorption.

The real part of the dielectric function represents the dispersion of the material, indicating how the phase velocity of light is altered as it travels through the material. It relates to the material's ability to polarize in response to an electric field and affects the refractive index. The static real dielectric constant $[\varepsilon_1(0)]$ was found to be 2.44 (2.36), 3.01 (2.96), and 4.01 (3.95), which confirms the highest dispersion at resonance frequency as shown in Fig. 7(a). The enhanced reactivity of a substance towards incident energy is attributed to the greater value of $\varepsilon_1(0)$ [89]. The examined substance is of high importance in the visible and ultraviolet ranges, as shown by the peak value of $\varepsilon_1(\omega)$. When the materials go from Cl to Br to I, there is a greater electronic impact, which causes the peak value (in eV) to fall. In addition, Penn's model links the band gap with static polarization in an inverse connection [90]:

$$\varepsilon_1(0) \approx 1 + \left[\frac{\hbar\omega_p}{E_g}\right]^2$$

The $\varepsilon_2(\omega)$ is presented in Fig. 7(b). It is a measure of how much energy from an incident light wave is absorbed by the material. This

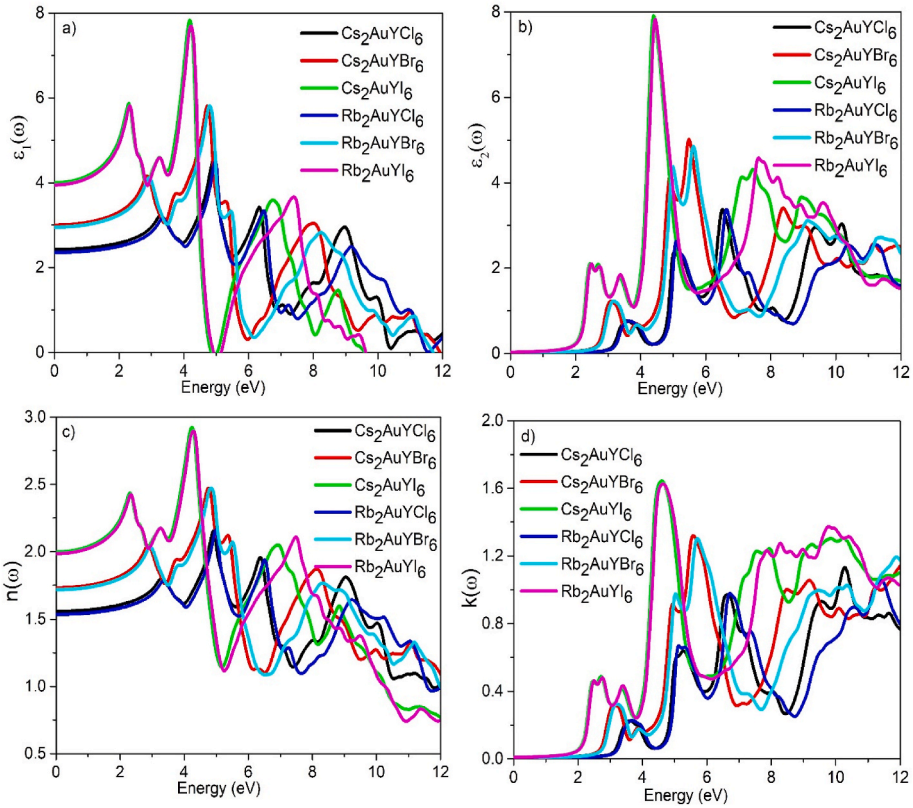

Fig. 7. a) $\varepsilon_1(\omega)$: real part of the dielectric function, b) $\boldsymbol{\varepsilon_2}$ **(ω)**: imaginary part of the dielectric function, c) ***n(ω)***: real part of refractive index, and d) ***k(ω)***: imaginary part of refractive index with photon energy for Cs_2AuYCl_6, Cs_2AuYBr_6, Cs_2AuYI_6, Rb_2AuYCl_6, Rb_2AuYBr_6, and Rb_2AuYI_6.

absorption can result in electronic excitations, which are fundamental to understanding the optical properties of the material. Peaks in $\varepsilon_2(\omega)$ typically arise from interband transitions, where electrons are excited from one energy band to another. The energy at which a peak occurs corresponds to the energy difference between the initial and final states involved in the transition [91]. The optical band gap is represented by a threshold energy value calculated by $\varepsilon_2(\omega)$ for the compounds under study, which is 2.92 (2.98), 2.38 (2.43), and 1.75 (1.80) eV. This value seems to be very close to the estimated electronic band gap. A slight overestimation of the optical band gap occurs in optical properties as a result of the calculation of its related potential. The present findings demonstrate a high degree of accuracy.

Utilizing $\varepsilon_1(\omega)$ and $\varepsilon_2(\omega)$, one may compute other optical parameters, such as complex refractive index, absorption coefficient $\alpha(\omega)$, real optical conductivity $\sigma(\omega)$, optical reflectivity $R(\omega)$, and electron energy loss $L(\omega)$. The formula for the complex refractive index is $n(\omega)$-$ik(\omega)$, where $k(\omega)$ is the imaginary component (extinction coefficient) and $n(\omega)$ is the real part (refractive index). The following equations calculated the optical constants using the conventional symbol meanings [63,92,93]:

$$n(\omega) = \frac{1}{\sqrt{2}}\left\{\sqrt{\varepsilon_1^2(\omega)+\varepsilon_2^2(\omega)} + \varepsilon_1(\omega)\right\}^{\frac{1}{2}}$$

$$k(\omega) = \frac{1}{\sqrt{2}}\left\{\sqrt{\varepsilon_1^2(\omega)+\varepsilon_2^2(\omega)} - \varepsilon_1(\omega)\right\}^{\frac{1}{2}}$$

$$\alpha(\omega) = \sqrt{2}\omega\left\{\sqrt{\varepsilon_1^2(\omega)+\varepsilon_2^2(\omega)} - \varepsilon_1(\omega)\right\}^{\frac{1}{2}}$$

$$\sigma(\omega) = \frac{\alpha(\omega) * n(\omega) * c}{4\pi} \approx \frac{\varepsilon_2(\omega)}{4\pi}$$

$$R(\omega) = \left|\frac{\sqrt{\varepsilon_1(\omega)+i\varepsilon_2(\omega)}-1}{\sqrt{\varepsilon_1(\omega)+i\varepsilon_2(\omega)}+1}\right|^2$$

$$L(\omega) = \frac{\varepsilon_2(\omega)}{\varepsilon_2^2(\omega)+\varepsilon_1^2(\omega)}$$

The real refractive index $n(\omega)$, determines the speed of light in the material and how much light bends or refracts as it moves from one medium to another. A higher refractive index means a slower light speed within the material and greater bending at interfaces. Fig. 7(c) shows the energy variation with $n(\omega)$. The n(ω) and $\varepsilon_1(\omega)$ show similar behavior in the following link [94]: $n^2(0) = \varepsilon_1(0)$. In the first absorption peak, the refractive index has static values of 1.55 (1.52), 1.74 (1.71), and 2.00 (1.97) and maximum values of 1.81 (1.78), 2.06 (2.03), and 2.45 (2.41), which are more suitable in comparison with silicon nitride (1.9) for solar cell applications [95]. Additionally, transparency (i.e., the lowest reflectivity and covalence nature) also exists due to the greater value of 1 of $n(\omega)$.

The extinction coefficient quantifies the extent to which a material absorbs and scatters light. It is associated with absorption processes, and a higher k value indicates stronger absorption by the following equations:

$$k(\omega) = \frac{\alpha(\omega)\,\lambda}{4\pi}$$

Fig. 7(d) illustrates that the visible-to-UV spectrum exhibits the highest extinction coefficient. It should be noticed that the greatest value of $k(\omega)$ is located approximately at the zero value of $\varepsilon_1(\omega)$.

The absorption coefficient, $\alpha(\omega)$, in semiconductors, is important to comprehend how materials take in photons and produce electron-hole pairs. It is crucial for understanding how much light is absorbed over a certain distance in the material, affecting applications in photovoltaic, sensors, and optical coatings. Devices like solar cells and photodiodes depend on this mechanism to function. The amount of incoming light that a substance absorbs is measured by its absorption coefficient. Stronger absorption is indicated by a greater absorption coefficient, which results in a more notable decrease in the transmitted light intensity. Higher-band gap materials are known to exhibit reduced absorption in the visible range of electromagnetic waves [54]; this is also present with the compound under study. In the visible photon energy range of 1.77–3.26 eV with corresponding wavelengths of 700 to 380 nm, the compounds of Cl, Br, and I-based Cs (Rb) exhibit maximum absorption coefficients of 0.23 (0.35) × 10^5 cm^{-1}, 1.01 (1.06) × 10^5 cm^{-1}, and 1.42 (1.48) × 10^5 cm^{-1}, respectively, as shown in Fig. 8(a) and (b). These results are very consistent with solar cell materials (Si, GaAs, InP, and CdTe) [96], DP-halide absorbing materials (Rb_2LiTlX_6 [79], Cs_2MGaBr_6 [55], and Cs_2KInX_6 [97], heterostructure [98] and 2D material monolayer [99]. Moreover, all compounds also exhibit a different increasing absorption coefficient in the UV spectrum of 4–12 eV, and the I-based compound always shows the maximum absorption peak as well. When an electron moves from its valence band (VB) to its conduction band (CB), a material with a greater absorption coefficient reacts more positively.

Inter-band shifts, which happen when photons absorb and excite electrons from the VB to the CB due to a breaking bond, are the primary source of optical conductivity in semiconductors. It provides insight into free carrier density and mobility. High optical conductivity indicates good electrical conduction, which is important for materials used in optoelectronic devices. We observe different optical conductivity peaks in the photon energy range of 0–12 eV, with the largest peak occurring at 6–8 eV and 7–11 eV for Cl, 5–6 eV and 8–10 eV for Br, and 4–5 eV and 7–11 eV for I-based compounds, as shown in Fig. 8(c). These peaks are quite interesting and may have applications in optoelectronics since they exist at different energy levels. The fact that both conductivity and absorption have minimum and maximum values in comparable regions validates the theory's concept and, therefore, the precision of the calculated outcomes.

The quantity of incoming light that is reflected at a semiconductor material's surface is known as optical reflectivity, $R(\omega)$. It is important for designing coatings and understanding the optical behavior of surfaces. High-reflectivity materials are used in mirrors and reflective coatings, while low-reflectivity is desired for anti-reflective coatings. Fig. 8(d) shows the optical reflectivity with incident energy variation and shows the inverse connection of absorbance. The static reflectivity values of Cs (Rb)-based halides (Cl, Br, and I) are 0.11 (0.10), 0.071 (0.069), and 0.046 (0.044), respectively, as shown in Table 5. The reflectivity expanded with increasing photon energy (eV), with the named compounds (both series of Cl, Br, and I) showing maximum reflectivity of 18%, 12%, and 8.5% in the visible range (1.75–3.10 eV). For comparison, the Si solar cell shows 20–13.9% reflectance with respect to 400–700 nm, which implies the more prominent nature of our studied compound [100].

Fig. 8(e) shows the energy loss of moving electrons within the material. It provides information about plasmon resonances and other collective oscillations of the electron gas. Peaks in the energy loss function are associated with plasma frequencies and can indicate the presence of free electrons [101]. It is observed that there is no static loss and that the losses begin at the corresponding threshold value, reaching the maximum value of 0.09 in the range of 0–4 eV for all compounds. Additionally, the losses increase with increasing energy, and they are high (50%) above 5 eV.

4. Conclusions

DFT analysis was used to look into the optimized structure of X_2AuYZ_6 (X = Cs/Rb; Z = Cl, Br, and I) for opto-electronic and thermoelectric power generators. The structural stability of the cubic phases is confirmed by tolerance factors ranging from 0.83 to 0.88 and

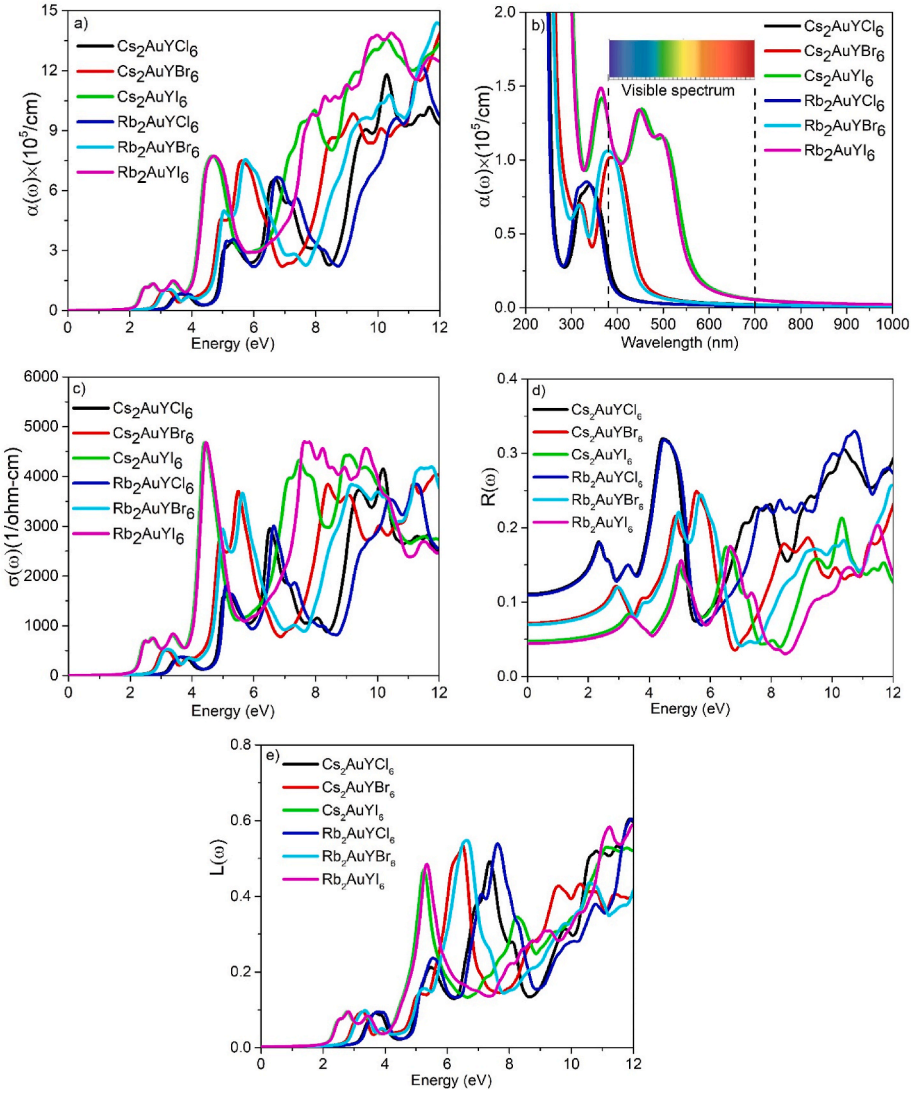

Fig. 8. a) and b) ***α(ω)***: Absorption coefficient w.r.t. eV and nm, c) σ(ω): Real optical conductivity, d) ***R(ω)***: Optical reflectivity, and e) ***L(ω)***: Electron energy loss of Cs_2AuYCl_6, Cs_2AuYBr_6, Cs_2AuYI_6, Rb_2AuYCl_6, Rb_2AuYBr_6, and Rb_2AuYI_6.

Table 5
Estimated the optical constants of the studied compounds.

Compound	$\varepsilon_1(0)$	*n (0)*	*R (0)*	$\alpha_{max}(\omega) \times 10^5\ cm^{-1}$
Cs_2AuYCl_6	2.44	1.55	11.14 %	0.23
Cs_2AuYBr_6	3.01	1.74	7.15 %	1.01
Cs_2AuYI_6	4.01	2.00	4.69 %	1.42
Rb_2AuYCl_6	2.36	1.52	10.86 %	0.35
Rb_2AuYBr_6	2.96	1.71	6.97 %	1.06
Rb_2AuYI_6	3.95	1.97	4.41 %	1.48

octahedral factors varying from 0.51 to 0.62. The formation energy of each compound by considering elements and competing phases establishes thermodynamic stability. The mechanical behavior verifies the ductility, as both the *B/G* ratio (>1.75) and *σ* (>0.26) surpass the critical limit. The decrease in band gap [2.82 (2.91), 2.35 (2.40), and 1.74 (1.78) eV] for Cs (Rb)-based halides was validated by tuning the indirect band gap with the replacement of halogens (Cl, Br, and I) in the L-X symmetry points. In CBM, the orbital contribution mainly comes from the Y-*d*, Au-*s*, and X-*p*, while the Au-*d* contributes to the VBM of the band structure. The lower effective charge carriers and state densities obtained signify the fabrication of clean energy technology. A negative dielectric constant in the UV range of photon energy allows for its use in optical systems such as filters, fiber optics, and shielding for electromagnetic devices. The refractive index at zero energy was evaluated to be 1.55 (1.52), 1.74 (1.71), and 2.00 (1.97) for Cs_2AuYCl_6 (Rb_2AuYCl_6), Cs_2AuYBr_6 (Rb_2AuYBr_6), and Cs_2AuYI_6 (Rb_2AuYI_6), respectively. These materials exhibit outstanding absorption values in the visible spectrum (in the 10^5 orders) and may be employed for opto-electronic applications. The positive see-beck coefficient confirmed the p-type semiconducting nature of the studied compounds. Comparatively, the ZT values of the Rb-based compounds with halides (Cl, Br, and I) were found to be higher than those of Cs, with values of 0.55 (0.51), 0.62 (0.53), and 0.75 (0.55) for Rb_2AuYCl_6 (Cs_2AuYCl_6), Rb_2AuYBr_6 (Cs_2AuYBr_6), and Rb_2AuYI_6 (Cs_2AuYI_6), respectively, recorded at 300 K. Finally, the narrow band gap compounds, such as X_2AuYI_6 (X = Cs, Rb), make them efficient absorbers of sunlight and are suitable for waste heat management through electricity generation. Therefore, these studies emphasize the significance of double perovskite halides for optoelectronic and thermoelectric applications, paving the way for future clean energy devices.

CRediT authorship contribution statement

S. Mahmud: Writing – original draft, Validation, Methodology, Formal analysis, Data curation, Conceptualization. **M.M. Hossain:**

Writing – review & editing, Validation. **M.M. Uddin:** Writing – review & editing, Validation. **M.A. Ali:** Validation, Supervision, Software, Formal analysis, Conceptualization, Writing – review & editing.

Declaration of competing interest

The authors declare that they have no known competing financial interests or personal relationships that could have appeared to influence the work reported in this paper.

Data availability

Data will be made available on request.

Acknowledgments

This work was carried out with the aid of a grant (grant number: 21-378 RG/PHYS/AS_G -FR3240319526) from UNESCO-TWAS and the Swedish International Development Co-operation Agency (SIDA). The views expressed herein do not necessarily represent those of UNESCO-TWAS, SIDA, or its Board of Governors. **S. Mahmud** expresses gratitude to the University Grants Commission (UGC) of Bangladesh for providing financial support to conduct this research under the **Ph.D. Fellowship program 2022-23**.

Appendix A. Supplementary data

Supplementary data to this article can be found online at https://doi.org/10.1016/j.jpcs.2024.112298.

References

[1] S.A. Dar, B. Want, Direct band gap double perovskite halide $Cs_2ScInCl_6$ for optoelectronic applications—a first principle study, Comput. Condens. Matter 33 (August) (2022) e00736, https://doi.org/10.1016/j.cocom.2022.e00736.
[2] S. Liu, et al., Boost the efficiency of nickel oxide-based formamidinium-cesium perovskite solar cells to 21% by using coumarin 343 dye as defect passivator, Nano Energy 94 (2022) 106935.
[3] Y. Chen, L. Zhang, Y. Zhang, H. Gao, H. Yan, Large-area perovskite solar cells–a review of recent progress and issues, RSC Adv. 8 (19) (2018) 10489–10508.
[4] M. Saliba, et al., Cesium-containing triple cation perovskite solar cells: improved stability, reproducibility and high efficiency, Energy Environ. Sci. 9 (6) (2016) 1989–1997.
[5] L. Wang, K. Wang, B. Zou, Pressure-induced structural and optical properties of organometal halide perovskite-based formamidinium lead bromide, J. Phys. Chem. Lett. 7 (13) (2016) 2556–2562.
[6] A. Richter, M. Hermle, S.W. Glunz, Reassessment of the limiting efficiency for crystalline silicon solar cells, IEEE J. Photovoltaics 3 (4) (2013) 1184–1191.
[7] M.A. Rehman, J. ur Rehman, M.B. Tahir, Density functional theory study of structural, electronic, optical, mechanical, and thermodynamic properties of halide double perovskites Cs_2AgBiX_6 (X = Cl, Br, I) for photovoltaic applications, J. Phys. Chem. Solid. 181 (February) (2023) 111443, https://doi.org/10.1016/j.jpcs.2023.111443.
[8] J. Kangsabanik, V. Sugathan, A. Yadav, A. Yella, A. Alam, Double perovskites overtaking the single perovskites: a set of new solar harvesting materials with much higher stability and efficiency, Phys. Rev. Mater. 2 (5) (2018) 55401.
[9] M. Roknuzzaman, et al., Electronic and optical properties of lead-free hybrid double perovskites for photovoltaic and optoelectronic applications, Sci. Rep. 9 (1) (2019) 718.
[10] G.K. Grandhi, et al., Lead-free cesium titanium bromide double perovskite nanocrystals, Nanomaterials 11 (6) (2021) 1458.
[11] C.N. Savory, A. Walsh, D.O. Scanlon, Can Pb-free halide double perovskites support high-efficiency solar cells? ACS Energy Lett. 1 (5) (2016) 949–955.
[12] X.-G. Zhao, et al., Design of lead-free inorganic halide perovskites for solar cells via cation-transmutation, J. Am. Chem. Soc. 139 (7) (2017) 2630–2638.
[13] E.T. McClure, M.R. Ball, W. Windl, P.M. Woodward, Cs_2AgBiX_6 (X= Br, Cl): new visible light absorbing, lead-free halide perovskite semiconductors, Chem. Mater. 28 (5) (2016) 1348–1354.
[14] A.J. Kale, R. Chaurasiya, A. Dixit, Inorganic lead-Free $Cs_2AuBiCl_6$ perovskite absorber and Cu_2O hole transport material based single-junction solar cells with 22.18% power conversion efficiency, Adv. Theory Simulations 4 (3) (2021) 2000224.
[15] A.U. Haq, G.M. Mustafa, M. Amin, S.M. Ramay, A. Mahmood, Ab-initio study of opto-electronic and thermoelectric properties of direct bandgap double perovskites Rb_2XGaBr_6 (X = Na, K), Int. J. Energy Res. 45 (6) (2021) 9241–9251, https://doi.org/10.1002/er.6455.
[16] S.A. Aldaghfag, A. Aziz, A. Younas, M. Yaseen, A. Murtaza, H.H. Hegazy, Investigation of electronic, optical and thermoelectric features of $X_2ScAgCl_6$ (X= K, Na) double perovskites for renewable energy applications, J. Solid State Chem. 312 (2022) 123179.
[17] M. Babaei, V. Ahmadi, G. Darvish, Opto-electro-mechanical properties of lead-free hybrid double perovskites Cs_2AgSbX_6 (X= Cl, Br, I) for solar cells: a first-principles study, J. Phys. Chem. Solid. 169 (2022) 110880.
[18] H. Wu, et al., Mixed-halide double perovskite Cs_2AgBiX_6 (X= Br, I) with tunable optical properties via anion exchange, ChemSusChem 14 (20) (2021) 4507–4515.
[19] N.R. Kumara, N.P. Mathewa, R. Radhakrishnana, Theoretical studies on lead-free halide double perovskites Cs_2AgSbX_6 (X= Cl, Br, I) for solar energy harvester, Mater. Today: Proc. 27 (2019) 561–564.
[20] S. Amraoui, A. Feraoun, M. Kerouad, Electronic and optical properties of the lead free halide double perovskites Cs_2AgBiX_6 (X= F, Cl, Br and I) for the photovoltaic and optoelectronic applications, Inorg. Chem. Commun. 140 (2022) 109395.
[21] N.H. Alotaibi, Frist principle study of double perovskites Cs_2AgSbX_6 (X= Cl, Br, I) for solar cell and renewable energy applications, J. Phys. Chem. Solid. 171 (2022) 110984.
[22] M.A. Ghebouli, T. Chihi, B. Ghebouli, M. Fatmi, Study of the structural, elastic, electronic and optical properties of lead free halide double perovskites Cs_2AgBiX_6 (X= Br, Cl), Chin. J. Phys. 56 (1) (2018) 323–330.
[23] M.N. Tripathi, A. Saha, S. Singh, Structural, elastic, electronic and optical properties of lead-free halide double perovskite Cs_2AgBiX_6 (X= Cl, Br, and I), Mater. Res. Express 6 (11) (2019) 115517.
[24] H.H. Hegazy, G.M. Mustafa, A. Nawaz, N.A. Noor, A. Dahshan, I. Boukhris, Tuning of direct bandgap of Rb_2ScTlX_6 (X = Cl, Br, I) double perovskites through halide ion substitution for solar cell devices, J. Mater. Res. Technol. 19 (2022) 1271–1281, https://doi.org/10.1016/j.jmrt.2022.05.082.
[25] G. Volonakis, et al., Lead-free halide double perovskites via heterovalent substitution of noble metals, J. Phys. Chem. Lett. 7 (7) (2016) 1254–1259.
[26] S. Mahmud, M.A. Ali, M.M. Hossain, M.M. Uddin, DFT aided prediction of phase stability, optoelectronic and thermoelectric properties of A_2AuScX_6 (A= Cs, Rb; X= Cl, Br, I) double perovskites for energy harvesting technology, Vacuum (2023) 112926.
[27] W. Shockley, H.J. Queisser, Detailed balance limit of efficiency of p-n junction solar cells, J. Appl. Phys. 32 (3) (1961) 510–519, https://doi.org/10.1063/1.1736034.
[28] N.H. Alotaibi, et al., Journal of Solid State Chemistry DFT study of double perovskites Cs_2AgBiX_6 (X = Cl , Br): an alternative of hybrid perovskites, J. Solid State Chem. 313 (June) (2022) 123353, https://doi.org/10.1016/j.jssc.2022.123353.
[29] N. Erum, J. Ahmad, M.A. Iqbal, M. Ramzan, DFT insights of mechanical, optoelectronic and thermoelectric properties for Cs_2ScTlX_6 (X = Cl, Br, I) double perovskites, Opt. Quant. Electron. 55 (4) (2023) 1–15, https://doi.org/10.1007/s11082-022-04538-2.
[30] A. Ayyaz, et al., DFT exploration of elastic, optoelectronic, and thermoelectric properties of stable and eco-friendly double perovskites Cs_2YAuX_6 (X= Cl, Br) for green energy applications, J. Phys. Chem. Solid. 188 (2024) 111936.
[31] E. Haque, M.A. Hossain, Origin of ultra-low lattice thermal conductivity in Cs_2BiAgX_6 (X = Cl, Br) and its impact on thermoelectric performance, J. Alloys Compd. 748 (2018) 63–72, https://doi.org/10.1016/j.jallcom.2018.03.137.
[32] Q. Mahmood, et al., Tunning of band gap of double perovskites halides Rb_2CuSbX_6 (X= Cl, Br, I) for solar cells and energy harvesting, Mater. Sci. Eng. B 286 (2022) 116088.
[33] M.A. Ali, et al., Appealing perspectives of structural, electronic, mechanical, and thermoelectric properties of $Tl_2(Se, Te)Cl_6$ vacancy-ordered double perovskites, J. Phys. Chem. Solid. 159 (2021) 110258.
[34] M. Sajjad, Q. Mahmood, N. Singh, J.A. Larsson, Ultralow lattice thermal conductivity in double perovskite Cs_2PtI_6: a promising thermoelectric material, ACS Appl. Energy Mater. 3 (11) (2020) 11293–11299.
[35] K. Schwarz, DFT calculations of solids with LAPW and WIEN2k, J. Solid State Chem. 176 (2) (2003) 319–328.
[36] J.P. Perdew, K. Burke, M. Ernzerhof, Generalized gradient approximation made simple, Phys. Rev. Lett. 77 (18) (1996) 3865.
[37] P. Vinet, J.H. Rose, J. Ferrante, J.R. Smith, Universal features of the equation of state of solids, J. Phys. Condens. Matter 1 (11) (1989) 1941.
[38] F. Tran, P. Blaha, Accurate band gaps of semiconductors and insulators with a semilocal exchange-correlation potential, Phys. Rev. Lett. 102 (22) (2009) 226401.
[39] G.K.H. Madsen, J. Carrete, M.J. Verstraete, BoltzTraP2, a program for interpolating band structures and calculating semi-classical transport coefficients, Comput. Phys. Commun. 231 (2018) 140–145, https://doi.org/10.1016/j.cpc.2018.05.010.
[40] M. Jamal, M. Bilal, I. Ahmad, S. Jalali-Asadabadi, IRelast package, J. Alloys Compd. 735 (2018) 569–579.
[41] M.D. Segall, et al., First-principles simulation: ideas, illustrations and the CASTEP code, J. Phys. Condens. Matter 14 (11) (2002) 2717.
[42] M.W. Lufaso, P.M. Woodward, Jahn-Teller distortions, cation ordering and octahedral tilting in perovskites, Acta Crystallogr. Sect. B Struct. Sci. 60 (1) (2004) 10–20, https://doi.org/10.1107/S0108768103026661.
[43] J. Akhtar, M. Aamir, M. Sher, Chapter 2 - organometal lead halide perovskite, in: S. Thomas, A. Thankappan (Eds.), Perovskite Photovoltaics, Academic Press, 2018, pp. 25–42, https://doi.org/10.1016/B978-0-12-812915-9.00002-2.
[44] A.E. Fedorovskiy, N.A. Drigo, M.K. Nazeeruddin, The role of Goldschmidt's tolerance factor in the formation of A_2BX_6 double halide perovskites and its optimal range, Small Methods 4 (5) (2020) 1900426.

[45] R.D. Shannon, Revised effective ionic radii and systematic studies of interatomic distances in halides and chalcogenides, Acta Crystallogr. Sect. A Cryst. physics, diffraction, Theor. Gen. Crystallogr. 32 (5) (1976) 751–767.

[46] S. Burger, M.G. Ehrenreich, G. Kieslich, Tolerance factors of hybrid organic–inorganic perovskites: recent improvements and current state of research, J. Mater. Chem. A 6 (44) (2018) 21785–21793.

[47] T. Tang, D. Hu, X. Zhao, L. Li, Y. Tang, First-principles study on the mechanical, electronic and optical properties of double halide perovskite Cs_2TlSbX_6 (X = Cl, Br, I), Phys. Scripta 97 (12) (Nov. 2022) 125821, https://doi.org/10.1088/1402-4896/ac9ff7.

[48] X. Du, D. He, H. Mei, Y. Zhong, N. Cheng, Insights on electronic structures, elastic features and optical properties of mixed-valence double perovskites $Cs_2Au_2X_6$ (X= F, Cl, Br, I), Phys. Lett. 384 (8) (2020) 126169.

[49] S. Kirklin, et al., The open quantum materials database (OQMD): assessing the accuracy of DFT formation energies, npj Comput. Mater. 1 (October) (2015), https://doi.org/10.1038/npjcompumats.2015.10.

[50] A. Jain, et al., Commentary: the Materials Project: a materials genome approach to accelerating materials innovation, Apl. Mater. 1 (1) (2013).

[51] M. Markov, et al., Semi-metals as potential thermoelectric materials, Sci. Rep. 8 (1) (2018) 9876.

[52] S.A. Dar, B. Want, DFT study of structural, mechanical, and opto-electronic properties of scadium-based halide double perovskite $Cs_2ScInBr_6$ for optoelectronic applications, Micro and Nanostructures 170 (2022) 207370.

[53] A.M. Mebed, S. Al-Qaisi, M.A. Ali, Study of optoelectronic and thermoelectric properties of double perovskites Rb_2AgBiX_6 (X= Br, I): by DFT approach, Eur. Phys. J. Plus 137 (8) (2022) 1–8.

[54] M. Nabi, D.C. Gupta, Potential lead-free small band gap halide double perovskites Cs_2CuMCl_6 (M= Sb, Bi) for green technology, Sci. Rep. 11 (1) (2021) 12945.

[55] M.Y. Sofi, M.S. Khan, J. Ali, M.A. Khan, Exploring the lead-free halide Cs_2MGaBr_6 (M = Li, Na) double perovskites for sustainable energy applications, Sci. Rep. 14 (1) (2024) 5520.

[56] A.J. Hong, C.L. Yuan, J.M. Liu, Quaternary compounds Ag_2XYSe_4 (X= Ba, Sr; Y= Sn, Ge) as novel potential thermoelectric materials, J. Phys. D Appl. Phys. 53 (11) (2020) 115302.

[57] F. Qi, X. Fu, L. Meng, C.-Z. Lu, Exploring High-Performance All-Inorganic perovskite materials for Next-Generation photovoltaic Applications: a theoretical study on Cs_2TlBiX_6 (X= Cl, Br, I), Comput. Theor. Chem. (2024) 114500.

[58] B. Yang, et al., Lead-free direct band gap double-perovskite nanocrystals with bright dual-color emission, J. Am. Chem. Soc. 140 (49) (2018) 17001–17006.

[59] G.M. Mustafa, et al., Study of optoelectronic, thermoelectric, mechanical properties of double perovskites Cs_2AgAsX_6 (X= cl, br, I) for solar cells and energy harvesting, Opt. Quant. Electron. 55 (6) (2023) 527.

[60] T. Saha, M.M.H. Babu, M. Arifuzzaman, J. Podder, Thermodynamic and dynamic stability in a new potential $Cs_2AgAsCl_6$ perovskite: insight from DFT study, Phys. Chem. Chem. Phys. 24 (43) (2022) 26609–26621.

[61] F. Hamioud, G.S. AlGhamdi, S. Al-Omari, A.A. Mubarak, Ab initio investigation of the structural, electronic, magnetic and optical properties of the perovskite $TlMnX_3$ (X= F, Cl) compounds, Int. J. Mod. Phys. B 30 (7) (2016) 1650031.

[62] A.J. Deotale, R.V. Nandedkar, Correlation between particle size, strain and band gap of iron oxide nanoparticles, Mater. Today Proc. 3 (6) (2016) 2069–2076.

[63] L. Schade, et al., Structural and optical properties of $Cs_2AgBiBr_6$ double perovskite, ACS Energy Lett. 4 (1) (2018) 299–305.

[64] Y. Zhou, G. Long, Low density of conduction and valence band states contribute to the high open-circuit voltage in perovskite solar cells, J. Phys. Chem. C 121 (3) (2017) 1455–1462, https://doi.org/10.1021/acs.jpcc.6b10914.

[65] M. Wuttig, et al., Halide perovskites: advanced photovoltaic materials empowered by a unique bonding mechanism, Adv. Funct. Mater. 32 (2) (2022) 2110166.

[66] M. Yaseen, et al., Phase transition and thermoelectric properties of cubic $KNbO_3$ under pressure: DFT approach, J. Mater. Res. Technol. 11 (2021) 2106–2113.

[67] A.H. Reshak, Transport properties of Co-based Heusler compounds Co_2VAl and Co_2VGa: spin-polarized DFT+ U, RSC Adv. 6 (59) (2016) 54001–54012.

[68] D.T. Morelli, G.A. Slack, High lattice thermal conductivity solids, in: High Thermal Conductivity Materials, Springer, 2006, pp. 37–68.

[69] S. Ohta, T. Nomura, H. Ohta, K. Koumoto, High-temperature carrier transport and thermoelectric properties of heavily La-or Nb-doped $SrTiO_3$ single crystals, J. Appl. Phys. 97 (3) (2005).

[70] G. Ding, G. Gao, K. Yao, High-efficient thermoelectric materials: the case of orthorhombic IV-VI compounds, Sci. Rep. 5 (1) (2015) 9567.

[71] W. Kim, Strategies for engineering phonon transport in thermoelectrics, J. Mater. Chem. C 3 (40) (2015) 10336–10348.

[72] S. Yousuf, D.C. Gupta, Investigation of electronic, magnetic and thermoelectric properties of Zr_2NiZ (Z= Al, Ga) ferromagnets, Mater. Chem. Phys. 192 (2017) 33–40.

[73] J.A. Cooley, et al., High seebeck coefficient and unusually low thermal conductivity near ambient temperatures in layered compound $Yb_{2-x}Eu_xCdSb_2$, Chem. Mater. 30 (2) (2017) 484–493.

[74] T.H. Geballe, G.W. Hull, Seebeck effect in silicon, Phys. Rev. 98 (4) (1955) 940.

[75] L. Yang, et al., High thermoelectric figure of merit of porous Si nanowires from 300 to 700 K, Nat. Commun. 12 (1) (2021) 3926.

[76] L. Li, et al., p53 regulation of ammonia metabolism through urea cycle controls polyamine biosynthesis, Nature 567 (7747) (2019) 253–256.

[77] L. Zheng, et al., Enhanced thermoelectric performance of F4-TCNQ doped $FASnI_3$ thin films, J. Mater. Chem. A 8 (47) (2020) 25431–25442.

[78] F. Qian, et al., Enhanced thermoelectric performance in lead-free inorganic $CsSn_{1-x}Ge_xI_3$ perovskite semiconductors, J. Phys. Chem. C 124 (22) (2020) 11749–11753.

[79] M. Manzoor, et al., Probing direct bandgap of double perovskites Rb_2LiTlX_6 (X = Cl, Br) and optoelectronic characteristics for Solar cell applications: DFT calculations, J. Mater. Res. Technol. 18 (2022) 4775–4785, https://doi.org/10.1016/j.jmrt.2022.04.073.

[80] K. Assiouan, et al., Theoretical investigation of Rb_2AuBiX_6 (X= Br, cl, F) double perovskite for thermoelectric and optoelectronic applications, J. Phys. Chem. Solid. (2024) 111890.

[81] H.A. Alburaih, N.A. Noor, A. Laref, M. Musa Saad H.-E, Investigation of mechanical, optoelectronic, and thermoelectric properties of double perovksites Li_2CuBiZ_6 (Z = Cl, Br, I) for solar cell applications, Sol. Energy 264 (2023) 112079, https://doi.org/10.1016/j.solener.2023.112079.

[82] S. Maqsood, G. Murtaza, N.A. Noor, R. Neffati, S. Nazir, A. Laref, First-principle investigation of thermoelectric and optoelectronic properties of Rb_2KScI_6 and Cs_2KScI_6 double perovskite for solar cell devices, J. Mater. Res. Technol. 21 (2022) 841–849, https://doi.org/10.1016/j.jmrt.2022.09.073.

[83] M.Z. Kazim, et al., Lead-free Cs_2InAsX_6 (X= Cl, Br) halide double perovskites: a DFT perspective on their potential for sustainable energy applications, J. Phys. Chem. Solid. (2024) 111954.

[84] S.H. Shah, et al., Comprehensive study of structural, elastic, electronic, optical, and thermoelectric properties of Rb_2NaTlZ_6 (Z = Cl, Br, and I) by DFT, Mater. Sci. Semicond. Process. 178 (2024) 108400.

[85] J. Brorsson, et al., Efficient calculation of the lattice thermal conductivity by atomistic simulations with ab initio accuracy 2100217 (2022) 1–13, https://doi.org/10.1002/adts.202100217.

[86] H. Ehrenreich, M.H. Cohen, Self-consistent field approach to the many-electron problem, Phys. Rev. 115 (4) (1959) 786–790, https://doi.org/10.1103/PhysRev.115.786.

[87] V. Lucarini, J.J. Saarinen, K.-E. Peiponen, E.M. Vartiainen, Kramers-Kronig Relations in Optical Materials Research, vol. 110, Springer Science & Business Media, 2005.

[88] A. Kojima, K. Teshima, Y. Shirai, T. Miyasaka, Organometal halide perovskites as visible-light sensitizers for photovoltaic cells, J. Am. Chem. Soc. 131 (17) (2009) 6050–6051.

[89] L. Azzouz, et al., Structural, electronic and optical properties of $ABTe_2$ (A = Li, Na, K, Rb, Cs and B = Sc, Y, La): insights from first-principles computations, J. Solid State Chem. 279 (2019) 120954.

[90] D.R. Penn, Wave-number-dependent dielectric function of semiconductors, Phys. Rev. 128 (5) (1962) 2093.

[91] A. Bafekry, et al., Electronic, optical and thermoelectric properties of a novel two-dimensional SbXY (X= Se, Te; Y= Br, I) family: ab initio perspective, Phys. Chem. Chem. Phys. 23 (45) (2021) 25866–25876.

[92] S.N. Behilil, et al., First-principles prediction of optoelectronic and thermoelectric properties of novel materials A_2PdCl_6 for Photovoltaic Applications, Comput. Condens. Matter 38 (October 2023) (2024) e00869, https://doi.org/10.1016/j.cocom.2023.e00869.

[93] A. Mera, M.A. Rehman, Z. ur Rehman, First-principles calculations to investigate the physical properties of lead-free double perovskites Cs_2AgXCl_6 (X = P, Co, As, Cd) for optoelectronic applications, Chin. J. Phys. 87 (June 2023) (2024) 268–283, https://doi.org/10.1016/j.cjph.2023.11.005.

[94] Z.-J. Liu, C.-R. Zhang, X.-W. Sun, L. Wang, T. Song, J.-H. Qi, Structural, electronic and optical properties of the tetragonal phase of $CaSiO_3$ perovskite under pressure: first-principles calculations, Mod. Phys. Lett. B 25 (1) (2011) 41–52.

[95] A. El Amrani, et al., Determination of the suitable refractive index of solar cells silicon nitride, Superlattice. Microst. 73 (2014) 224–231, https://doi.org/10.1016/j.spmi.2014.05.025.

[96] J. Xie, F. Liu, K. Yan, Chapter 5 - perovskite solar cells processed by solution nanotechnology, in: F. Gao (Ed.), Advanced Nanomaterials for Solar Cells and Light Emitting Diodes, Micro and Nano Technologies, Elsevier, 2019, pp. 119–174, https://doi.org/10.1016/B978-0-12-813647-8.00005-9.

[97] I. Hamideddine, H. Jebari, H. Ez-Zahraouy, Insights into optoelectronic behaviors of novel double halide perovskites Cs_2KInX_6 (X = Br, Cl, I) for energy harvesting: first principal calculation, Phys. B Condens. Matter 677 (December 2023) (2024) 415699, https://doi.org/10.1016/j.physb.2024.415699.

[98] S.A. Essaa, H.R. Jappor, Tunable photocatalytic and optoelectronic properties of SiTe/SiH heterostructure as a photocatalytic water splitting with high hydrogen production, J. Phys. Chem. Solid. (2024) 112125.

[99] A.O.M. Almayyali, H.R. Jappor, $PbBi_2Se_4$ monolayer: a new 2D material with outstanding electronic, photocatalytic, and optical properties, Solid State Sci. 150 (2024) 107483.

[100] F. Nigo, M. Hashida, M. Tsukamoto, S. Sakabe, M. Kusaba, Reflectance and crystallinity of silicon solar cells with LIPSS produced by XeCl excimer laser pulses, Appl. Phys. A 126 (2) (2020) 1–5, https://doi.org/10.1007/s00339-020-3305-2.

[101] A. Bafekry, et al., Semiconducting chalcogenide alloys based on the (Ge, Sn, Pb) (S, Se, Te) formula with outstanding properties: a first-principles calculation study, ACS Omega 6 (14) (2021) 9433–9441.